JGR Oceans

RESEARCH ARTICLE
10.1029/2023JC020610

Mixing and Water Mass Transformation Over Discovery Bank, in the Weddell-Scotia Confluence of the Southern Ocean

J. Alexander Brearley[1], James B. Girton[2], Natasha S. Lucas[1], Andreas M. Thurnherr[3], E. Povl Abrahamsen[1], Michael P. Meredith[1], Andrew S. Meijers[1], and Hugh J. Venables[1]

[1]British Antarctic Survey, Cambridge, UK, [2]Applied Physics Laboratory, University of Washington, Seattle, WA, USA, [3]Lamont Doherty Earth Observatory, Columbia University, New York, NY, USA

Abstract The South Scotia Ridge, in the Atlantic sector of the Southern Ocean, is a key region for water mass modification. It is the location of the Weddell-Scotia Confluence, an area of reduced stratification which separates the Weddell Gyre to the south and the Antarctic Circumpolar Current to the north, and which receives input of shelf waters from the tip of the Antarctic Peninsula. To elucidate the transformations over the ridge, we focus on one of its largest seamounts, Discovery Bank, which has previously been observed as hosting a stratified Taylor column that retains water for months to years, during which time water masses are entrained from north and south of the Weddell Front and steadily mixed. Data from ship-deployed sensors and autonomous platforms are analyzed to quantify and understand the diapycnal mixing, heat fluxes and water mass transformations over the bank. Ocean glider and free-profiling drifting float data show that the mid-depth temperature maximum of the Circumpolar Deep Water (CDW) is eroded between the northern and southern sides of the bank, while diapycnal diffusivity is enhanced by up to an order-of-magnitude over its steeply sloping portions. This is accompanied by heat fluxes from the CDW layer being increased by up to a factor of six, which may contribute to a reduction in mid-depth stratification. Tidal model analysis shows that the southern side of the bank hosts strong barotropic to baroclinic energy conversion (>150 N m^{-2}), emphasizing the role of internal tides in modulating water mass transformations in the Confluence.

Plain Language Summary The Weddell-Scotia Confluence region, in the South Atlantic sector of the Southern Ocean, is a zone where ocean waters from the Antarctic Circumpolar Current to the north, the Weddell Sea to the south, and the Antarctic Peninsula to the west, come together and interact. In this paper, observations from a research ship, an autonomous underwater glider, and free-drifting ocean floats are used to characterize the mixing between these different sources of water, and to understand what impact this mixing has on the downstream vertical structure of the water column. The results show that an anticlockwise circulation of waters occurs around a large underwater seamount in the region, causing the waters there to be trapped for months to years. In addition, interaction with the steeply sloping undersea topography generates particularly strong mixing between these different waters through the action of tides, which helps to sustain the characteristic low vertical density gradients present in the region. These processes have important implications for both the movement of mid-depth waters south into the circulation of the Weddell Sea, and likely also for the supply of nutrients to the productive surface layer of the ocean.

Key Points:

- New observations reveal enhanced mixing rates and mid-depth heat fluxes over one of the largest seamounts of the South Scotia Ridge
- This enhanced mixing may help to sustain the mid-depth stratification minimum found in the Weddell Scotia Confluence
- Results from a tidal model show high rates of barotropic to baroclinic tidal energy conversion over steeply sloping parts of the bank

Correspondence to:
J. A. Brearley,
jambre@bas.ac.uk

Citation:
Brearley, J. A., Girton, J. B., Lucas, N. S., Thurnherr, A. M., Abrahamsen, E. P., Meredith, M. P., et al. (2024). Mixing and water mass transformation over discovery bank, in the Weddell-Scotia confluence of the Southern Ocean. *Journal of Geophysical Research: Oceans*, *129*, e2023JC020610. https://doi.org/10.1029/2023JC020610

Received 2 NOV 2023
Accepted 27 AUG 2024

Author Contributions:

Conceptualization: J. Alexander Brearley
Data curation: E. Povl Abrahamsen
Formal analysis: Natasha S. Lucas, Andreas M. Thurnherr
Funding acquisition: J. Alexander Brearley, Michael P. Meredith
Investigation: E. Povl Abrahamsen
Methodology: J. Alexander Brearley, James B. Girton, Natasha S. Lucas, Andreas M. Thurnherr
Project administration: J. Alexander Brearley, Andrew S. Meijers
Resources: Hugh J. Venables
Visualization: J. Alexander Brearley, Andreas M. Thurnherr
Writing – original draft: J. Alexander Brearley
Writing – review & editing: J. Alexander Brearley, James B. Girton,

1. Introduction

The South Scotia Ridge (hereafter known as "the ridge"), located in the South Atlantic sector of the Southern Ocean (Figure 1), is a region of complex topography that separates the cyclonic Weddell Gyre to the south (Vernet et al., 2019) from the eastward-traveling Antarctic Circumpolar Current (ACC) to the north (Rintoul et al., 2001). While named as a coherent feature, the ridge in reality comprises a large number of individual seamounts, which rise from the abyssal Weddell Sea, over 4,000 m deep, to shallower than 500 m. Above the ridge is found the Weddell Scotia Confluence (hereafter known as "the confluence"), usually defined as the region between the Southern Boundary of the ACC to the north, and the Weddell Front to the south (Patterson & Sievers, 1980). Though originally thought to contain simply an admixture of Weddell Sea and ACC waters, it was observed that the confluence is also characterized by a mid-depth stratification minimum around and above the level of the CDW layer (200–400 m), implying the entrainment of shelf waters from the tip of the Antarctic Peninsula into the confluence (Whitworth et al., 1994).

Natasha S. Lucas, Andreas M. Thurnherr, E. Povl Abrahamsen, Michael P. Meredith, Andrew S. Meijers, Hugh J. Venables

The ridge is also known as a region where strong meridional exchanges of water occur, which are key to the configuration of both the upper and lower limbs of the Southern Ocean overturning circulation. At intermediate and upper levels, the confluence is characterized by a general southward intrusion of Circumpolar Deep Water (CDW) from the ACC, with the lower component of this water mass penetrating into the gyre near its eastern boundary, before recirculating in the Weddell Sea (Vernet et al., 2019) and reaching the Filchner Ronne Ice Shelf at the southern end of the Weddell Sea (Davis et al., 2022). After extensive mixing and recirculation, this Warm Deep Water (WDW) can then intrude into the confluence from the south. The interaction of the CDW from the ACC to the north with this WDW from the south is a key feature of the Weddell Front, which generally sits over the southern slope of the ridge.

In the deepest levels, dense Antarctic Bottom Water (AABW), formed via complex ocean/ice interactions on the shelves of the Weddell Sea, is exported from the gyre, partly through deep gaps in the ridge, in particular Orkney Passage (Abrahamsen et al., 2019). After complex modification within these passages (Orsi et al., 1999; Polzin et al., 2014), the AABW enters the Scotia Sea to the north and replenishes the lower limb of the Atlantic Meridional Overturning circulation (AMOC). Recent observations have shown a decadal warming, freshening and contraction of this AMOC branch (Abrahamsen et al., 2019; Zhou et al., 2023).

The influence of topography on Southern Ocean circulation is well-documented (e.g., Naveira Garabato et al., 2004), both through its role in influencing the movement of stratified flows and in its impact on both isopycnal and diapycnal mixing. Previous observations from the ridge (Meredith et al., 2015) showed that many of the constituent seamounts support stratified Taylor columns, whereby water is trapped above the seamount to form a column that rotates anticyclonically while sitting in the background flow. This was evidenced through both the retention of an Argo float for over 4 years within the vicinity of Bruce Bank and Discovery Bank to the east of Orkney Passage, and from vessel-mounted Acoustic Doppler Current Profiler (ADCP) data that demonstrated a near full-depth anticyclonic vorticity around Discovery Bank. For the observed Burger number of the flow (0.25), which expresses the relative importance of local stratification to rotation, the critical height for stratified Taylor column formation, expressed as the ratio of scaled bump height to Rossby number (h_0/Ro), is around 2–3 (Huppert, 1975). For Discovery Bank, the observed value of h_0/Ro was over 2 orders of magnitude higher than this (up to 800). Using transient tracer data, retention and mixing of water within the column was demonstrated to be responsible for enhanced isopycnal mixing rates of 1,000–1,800 m^2s^{-1}, large enough to cause a significant local water mass transformation (Meredith et al., 2015).

Beyond the immediate vicinity of South Scotia Ridge, topography elsewhere within the Southern Ocean has been shown to significantly affect both large-scale flows and turbulent mixing. Both Sévellec et al. (2015) and Campbell et al. (2019) highlighted Taylor columns being present over seamounts of different scales, while Brearley et al. (2013) and Nikurashin and Ferrari (2010) highlighted that such seamounts can become loci of enhanced diapycnal mixing from either the interaction of deep-reaching ACC jets with topography, or from generation of internal tides. More broadly, a significant literature has amassed in the past decade over the impact of bathymetric obstacles in the Southern Ocean. Thompson and Sallée (2012) highlighted the important role played by ridges in cross-frontal exchange within the ACC, with up to 75% of floats crossing fronts occurring in the lee of bathymetry, accompanying an enhancement in baroclinic instability and eddy kinetic energy (EKE). Subsequent papers have highlighted the interaction between ACC meanders and topography in enhancing poleward fluxes of heat and other properties (Dufour et al., 2015; Foppert et al., 2017; Naveira Garabato et al., 2011), as well as strongly influencing EKE (Martínez-Moreno et al., 2021), vertical momentum transport, upwelling of CDW (Tamsitt et al., 2017) and subduction of carbon (Llort et al., 2018).

With such an array of processes potentially active over the ridge, a dedicated field campaign was launched under the UK ORCHESTRA program in 2019 to elucidate the key mixing and water mass transformation processes occurring over Discovery Bank, a 330 km long bank rising from 5,500 m to shallower than 500 m, to the east of Orkney Passage (Figure 1). Details of data collection and processing are outlined in Section 2, while the hydrography of the region from underwater glider and float data is detailed in Section 3. Section 4 discusses the observed diapycnal mixing rates over the bank from both float and microstructure profiler data, while Section 5 examines the likely mechanisms for the observed patterns of turbulent diffusivity, and the impact of this mixing and entrainment on the modification of water masses within the WSC. Conclusions are outlined in Section 6.

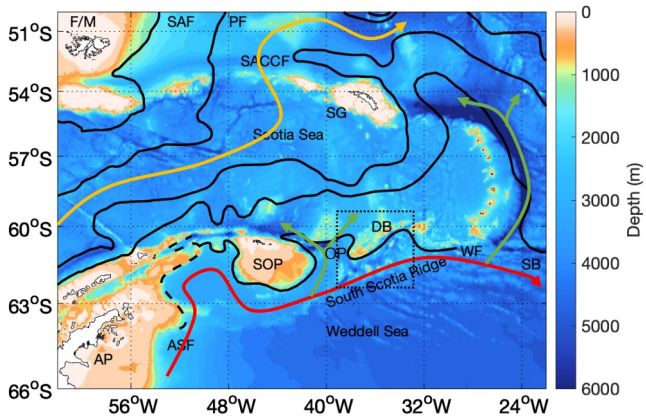

Figure 1. Hydrography of the Weddell Scotia Confluence, with 30 arc s GEBCO_2014 bathymetry and various features shown. F/M is Falkland Islands/Malvinas, SG is South Georgia, AP is Antarctic Peninsula, SOP is South Orkney Plateau, OP is Orkney Passage and DB is Discovery Bank (location of the field site). Fronts from Orsi et al. (1995) and Heywood et al. (2004) are shown, these being (north to south) the Subantarctic Front (SAF), the Polar Front (PF), the Southern Antarctic Circumpolar Current Front (SACCF), the Southern Boundary (SB), the Weddell Front (WF) and the Antarctic Slope Front (ASF). Schematic arrows of the near-surface circulation are shown, with the red arrow denoting the northern limb of the Weddell Gyre, the green arrows denoting outflows of dense water from the Weddell Sea and the yellow arrow denoting the ACC. The area displayed in Figure 2 is outlined with a dashed box.

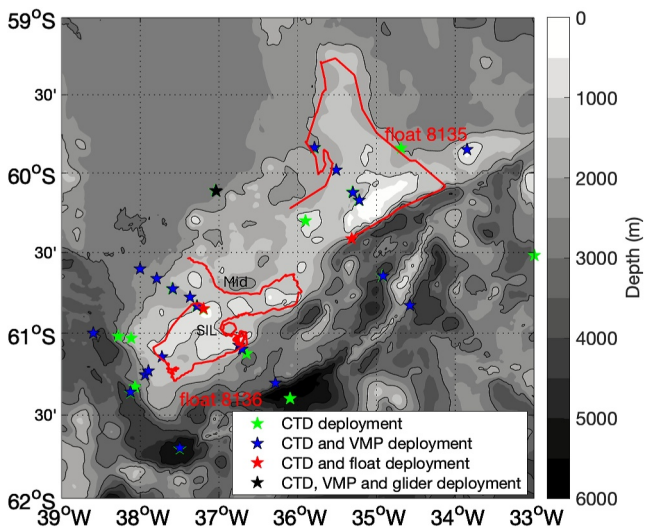

Figure 2. Map of Discovery Bank showing positions of CTDs and VMP, EM-APEX float and Slocum glider deployments. Bathymetry from the 30-arc s GEBCO_2014 grid is displayed, alongside the paths of the two floats (starting at the red starred positions). The position of the subinertial loops (SIL) and where the float crosses the midpoint of the ridge (Mid) is shown.

2. Data and Methods

2.1. Hydrographic Data

The hydrographic and acoustic data presented here were collected during a cruise on RRS James Clark Ross in February 2019. Full details of data collection are given in Brearley (2019). In brief, a Sea-Bird Scientific 9plus Conductivity-Temperature-Depth (CTD) instrument mounted on a rosette with 24 Niskin bottles was used to profile the full depth of the ocean at a range of locations that spanned the bank (Figure 2), with CTD temperatures calibrated using a SBE-35 high precision reference thermometer, and conductivities calibrated using discrete bottle samples analyzed on a Guildline Autosal 8400B salinometer. Resultant temperature (T) and absolute salinity (S) accuracy was 0.001°C and 0.002 g/kg respectively.

Alongside the CTD data, direct estimates of ocean velocity at each station were made using 300 kHz Teledyne/RDI Workhorse Monitor Lowered Acoustic Doppler Current Profilers (LADCPs). Data were collected in 8 m bins with a staggered 1.3/1.5 s ping rate for up-looking and down-looking instruments, before being processed using version IX 13 of the Matlab-based LDEO LADCP software. This incorporates the CTD time series to constrain the sound speed and LADCP depth, the GPS time series to constrain the barotropic velocities and the shipboard ADCP data to constrain the surface layer velocities. The mismatches with the shipboard ADCP were typically less than 0.06 m s^{-1}, indicating high-quality data on all casts. A summary of the CTD/LADCP data is supplied in Table 1.

2.2. Glider Data

A Teledyne Webb Research Slocum G2 glider (serial number 631) was deployed on 2 February 2019, at the location indicated in Figure 2, and incorporated a pumped Sea-Bird Scientific Glider Payload CTD, alongside other sensors. Only the CTD data were used here. The glider undertook a series of crossings of Discovery Bank and was recovered on 9 April 2019. After data download, a number of quality control steps were undertaken. T and S were bin-averaged onto 2 dbar levels and any spikes removed. The despiking was performed through a combination of an automatic neighborhood despiking, followed by a manual inspection of the individual profiles. In the neighborhood despiking, T and S values were removed if they fell outside the range $q_1 - 2(q_3 - q_1) < T/S < q_3 + 2(q_3 - q_1)$, where q_1 and q_3 are the lower and upper quartiles of the chosen range, respectively. In order to test for thermal lag effects, sequential upward and downward temperature profiles were compared using the SOCIB glider toolbox (Troupin et al., 2015). Owing to the CTD being pumped, thermal lag effects were very small and corrections required minimal. Finally, the corrected data were compared with high-quality CTDs obtained on RRS James Clark Ross at the start and end of deployment. A small conductivity drift (from +0.006 mS cm^{-1} at the start of the deployment to zero at the end of the deployment) was observed and the individual profiles corrected appropriately, with salinities recalculated. For both ship and glider CTD data, neutral density (γ^n) was calculated according to Jackett and McDougall (1997).

2.3. EM-APEX Float Data

Two Teledyne Webb Research Electromagnetic-APEX (EM-APEX) floats, serial numbers 8136 and 8135, were deployed on either flank of Discovery Bank on 1 and 2 February respectively (Figure 2). In addition to a Sea-Bird

Table 1
Summary Table of Times/Dates for Ship-Based Fieldwork and Glider/EM-APEX Float Profiles

Instrument type	Number of profiles	Start date of data collection (UTC)	End date of data collection (UTC)
Seabird 911+ conductivity-temperature-depth	34	31/01/2019 0248	08/02/2019 1253
Rockland VMP-5500 vertical microstructure profiler	22	31/02/2019 0248	08/02/2019 1116
Slocum 1,000 m-rated underwater glider (631)	832	02/02/2019 1136	09/04/2019 0722
EM-APEX float 8135	146	02/02/2019 2204	20/07/2019 1441
EM-APEX float 8136	586	01/02/2019 1825	24/05/2019 1908

Note. Full details are found in the cruise report (Brearley, 2019).

Scientific SBE41CP Argo CTD sensor measuring temperature, conductivity and pressure, these floats also measure horizontal water velocity by measuring the motionally-induced electric fields generated by the ocean currents moving through the vertical component of the Earth's magnetic field as the float ascends and descends through the water column. Float 8136 was programmed so that, after an initial period of high-frequency shallow sampling, it collected 6 profiles from the surface to 900 m over approximately an inertial period (13.4 hr—at 60°S the inertial period f is 13.8 hr), with each individual profile pair taking approximately 4.1 hr to complete, and the bursts separated by ∼12.8 hr. In contrast, float 8135 was configured to collect four profiles from the surface to 1,388 m over approximately an inertial period (13.9 hr), with each individual profile pair taking approximately 6 hr to complete, and the burst separated by 4.25 days. The initial intention was that the sparser sampling of float 8135 would permit multi-year sampling, but unfortunately the float did not survive beyond the onset of sea ice in mid-July 2019. CTD data from the initial float profiles were compared with calibrated ship-based CTD data at the time of deployment (See Section 2.1), but in both cases no adjustment to temperature or conductivity values were required.

Velocity measurements were derived from seawater voltages sensed by silver–silver chloride electrodes by demodulating the signal at the float's rotation rate and dividing by the local vertical geomagnetic field strength from the IGRF-13 model. For more details on the EM-APEX and motional induction technique, see Sanford et al. (2005, 1978), Sanford (1971). The EM-APEX rotation period was 8–12 s and is driven by external fins as the float profiled vertically at 10–14 cm s^{-1}. Demodulation was performed over sliding 50 s windows, using a convolution with on-board horizontal magnetometer measurements to extract the magnetic north and east component of the ambient electric field. This rotational demodulation was needed to separate the O(100 nV) motionally-induced signals from O(1 mV) electrode offsets which drift in a non-predictable way throughout the profile but with minimal variance at the rotation frequency. The precision of the voltage measurements translates to a velocity uncertainty well below 1 cm s^{-1} over most of the global ocean (exceeding this within a few degrees of the geomagnetic equator, where Fz, the vertical component of the Earth's geomagnetic field, vanishes).

The motionally-induced voltage includes contributions from both the local horizontal velocity at each depth (the motion of the float itself) and a depth-independent electric field driven by the barotropic flow, so additional information from the GPS-derived displacement of the float over the subsurface round-trip profile is needed to arrive at an absolute velocity measurement. This correction resulted in somewhat greater error in the absolute velocity (O (2 cm s^{-1})) than in estimates of relative velocity (O (0.5 cm s^{-1})). Errors computed from the 50 s residual RMS in the velocity demodulation were used to screen for wild points and are generally 0.2 cm s^{-1} or less, except where wave velocities add exponentially-increasing noise (and allow an estimate of significant wave height) near the surface.

To estimate dissipation of turbulent kinetic energy (ε), the Gregg-Henyey-Polzin (GHP) shear-strain parameterization was employed (Gregg, 1989; Henyey et al., 1986; Polzin et al., 1995), using the finescale strain and shear data from the floats. The GHP parameterization assumes that dissipation at molecular scales can be approximated by measuring the spectral content of the internal wave shear and strain. Several key limitations exist in the application of this technique, including that the internal wave field is stationary and that the field bears clear resemblance to a Garrett-Munk (GM) type spectrum (Garrett & Munk, 1975). Full details of the processing can be found in the Meyer et al. (2014) toolbox. In brief, estimates of buoyancy-frequency squared (N^2) were calculated from 3 m binned CTD data from the floats, and a reference N^2 (N^2_{ref}) was also calculated from a running mean N^2 of 20 profiles. Vertical shear was evaluated over the same depth intervals for each timestep, and wavenumber

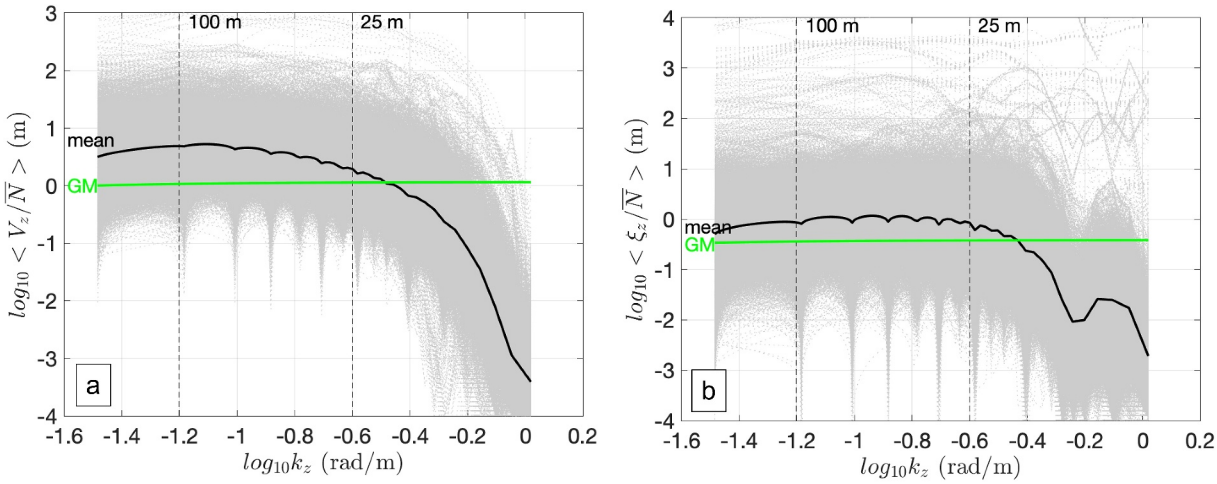

Figure 3. (a) Buoyancy normalized shear and (b) strain spectra for EM-APEX float 8136 (light gray), with chosen integration limits shown, and mean values shown in solid black alongside the GM spectrum (green).

spectra were then estimated from buoyancy normalized vertical shear $\langle V_z/N \rangle$, with a fast Fourier transform (fft) length of 64 (equating to 192 m) and 50% overlapping windows. Profiles of strain ξ for each profile were obtained as follows:

$$\xi = \frac{N^2 - N_{\mathrm{ref}}^2}{N_{\mathrm{ref}}^2} \tag{1}$$

and strain spectra $\langle \xi_z \rangle$ calculated following the same approach as for the buoyancy-normalized shear. The dissipation rate of turbulent kinetic energy ε is then quantified using the calculated shear spectra $\langle V_z/N \rangle$ as:

$$\varepsilon = \varepsilon_0 \frac{f}{f_0} \frac{\cosh^{-1}(N/f)}{\cosh^{-1}(N_0/f_0)} \frac{\langle V_z/\overline{N} \rangle^2}{\langle V_{z_{GM}}/N_0 \rangle^2} h_1(R_\omega) \tag{2}$$

In this equation, $\varepsilon_0 = 7.8 \times 10^{-10}$ W kg^{-1} is the background turbulent dissipation of a GM internal wave spectrum at latitude 30° in stratification $N_0 = 5.24 \times 10^{-3}$ rad s^{-1} (Garrett & Munk, 1975). The absolute values of the Coriolis parameter f at the latitude of interest (60°S), and at 30° (f_0) are 1.26×10^{-4} and 7.3×10^{-5} s^{-1} respectively.

The function h_1 (R_ω), which accounts for the dominant frequency in the observed wavefield, is defined as:

$$h_1(R_\omega) = \frac{3(R_\omega + 1)}{2\sqrt{2}R_\omega\sqrt{R_\omega - 1}} \tag{3}$$

and is a function of the shear-to-strain ratio R_ω (Polzin et al., 1995). R_ω is estimated for each overlapping window from the shear and strain spectra. We chose to evaluate both shear and strain spectra between 25 and 100 m wavelengths, being a compromise between the requirement for a fft of sufficient length to obtain enough spectral points in the integration, but not so long as to lose large quantities of data at the top and bottom of the profiles, where we believed important mixing processes may be occurring. It was observed that the shear and strain spectra were generally GM-like across this range, giving us confidence in the parameterization (Figure 3). The results were also tested using a longer fft length (128, equating to 384 m) and longer integration limits (both a fixed 75–200 m and a methodology that refines the lower wavelength of spectral integration by using the local value of N^2 for the individual data segment), but no significant difference in either the deployment mean value of ε or the variability was obtained. While a quantitative comparison with direct estimates of mixing from microstructure (see Section 2.4 below) was not possible due to differing times and positions of the individual profiles, further comment is made about the similarity of the overall patterns in Section 4.1 below.

The calculated rates of ϵ are used alongside the float CTD data to estimate the turbulent diffusivity κ, using the Osborn relation (Osborn, 1980):

$$\kappa = \Gamma \epsilon / N^2 \tag{4}$$

where Γ is the mixing coefficient defining the ratio of the final change in potential energy relative to the kinetic energy lost, taken to be the canonical value of 0.2 (Gregg et al., 2018; Oakey, 1982; Osborn & Cox, 1972). Finally, κ is used in conjunction with the float or ship CTD data to compute vertical heat fluxes, as follows:

$$Q = -\rho c_p \kappa \frac{\partial \Theta}{\partial z} \tag{5}$$

where c_p is the specific heat capacity of sea water (taken as 3,800 J kg^{-1} K^{-1}), ρ is the in-situ water density, and Θ is conservative temperature.

2.4. Vertical Microstructure Profiler Data

A Rockland Scientific VMP-5500 free-falling Vertical Microstructure Profiler (VMP) (serial number 107) was used to obtain profiles of TKE dissipation at a selection of the CTD stations outlined in Section 2.1. Full details are provided in the cruise report (Brearley, 2019), but in brief, 22 VMP profiles were collected over Discovery Bank, collecting velocity shear $\partial u/\partial z$ and temperature variance on centimeter scales. Assuming turbulence isotropy, ϵ_{micro} is given as follows:

$$\epsilon_{\text{micro}} = 15\nu\left(\overline{\partial u/\partial z}\right)^2 \tag{6}$$

where ν is the molecular viscosity (Oakey, 1982). For the VMP, velocity shear variances were computed every 0.5 dbar, using bin widths of 1 s, and sampling rate of 512 Hz. A modified version of the so-called "Goodman correction" was applied to correct for contamination of the microscale shear measurements by vibration of the instrument platform. Full details of this are provided in Appendix A.

Resultant dissipation values were subsequently interpolated onto a 2 dbar grid. Good quality data were found on all profiles except one, which was missing good-quality shear data below 635 m. Fall speeds of the instrument were around 63 cm s^{-1}, and noise levels on the better shear-1 probe around 2×10^{-11} W kg^{-1}, typically well below the noise floor of the observations. Shear-1 and shear-2 probes were evaluated for data quality on each cast —for those profiles with good quality on both probes a simple geometric mean of the dissipation rates was used.

2.5. Satellite Altimetry

In order to contextualize the hydrographic and velocity data, ¼ degree daily gridded sea surface height (SSH) and surface geostrophic velocities and mean absolute dynamic topography (Rio et al., 2011) were obtained from AVISO for the period of the glider and float deployments, before being time-averaged to examine the key features of the ACC fronts close to Discovery Bank during the period of interest. The AVISO product is based on an optimal interpolation of SSH anomaly derived from multiple satellite altimeters (see acknowledgments).

2.6. Tidal Velocities

Barotropic tidal velocities were extracted from the CATS 2008 (Circum-Antarctic Tidal Simulation) Oregon State University Tidal model (Egbert & Erofeeva, 2002) for the period of the float deployment using the Tidal Model Driver extraction tool for Matlab. The tidal velocities were evaluated over the region 59–61°S, 38–34°W as a mean for the whole deployment period (Table 1) and also along the float tracks at the times of the individual profiles.

2.7. Topography

Bathymetry data were extracted from the GEBCO_2014 30-arc s data set (Weatherall et al., 2015), for the purpose of computing gradients in bottom depth when estimating baroclinic conversion rates (Section 5). While some

multibeam data were collected on the ship survey, these were not used for this analysis as a regular complete grid was required for the conversion analysis.

3. Hydrography and Circulation

3.1. Hydrography

Along-track sections of conservative temperature Θ and absolute salinity *S* from the EM-APEX floats, and from two of the glider sections, are shown in Figure 4. Warm and salty Circumpolar Deep Water (CDW) is found below 150 m, with the temperature maximum generally found around 250 m. This is capped by the cold and relatively fresh Winter Water (WW), whose core is typically located around 100 m depth. Above this is the seasonal thermocline, which is gradually eroded during the float and glider deployments once the air-sea heat flux becomes negative during the austral autumn (fluxes not shown). This is accompanied by destratification that reaches into the WW layer and a deepening of the mixed layer from 70 to 120 m (Figures 4a and 4b). A gradual salinification of the surface layer occurs at the same time, presumably due to the effects of brine rejection as sea ice formation begins.

In addition to this temporal variability, significant spatial variability in hydrographic properties is also observed over Discovery Bank. The conservative temperature of the CDW temperature maximum Θ_{max} varies significantly between the individual glider and float profiles, but there is a strong tendency for those profiles to the north and west of the bank to have the highest Θ_{max} with maxima up to 1.5°C, compared with values of 0.5°C to 0.9°C over and on the southern flank of the bank. This pattern is seen clearly in both float 8136 (Figure 4c), where there is a rapid reduction in Θ_{max} as the float traverses the southern side of the bank (100–300 km along the baseline), and also in glider sections 1 and 2, where the profiles at the northern edge of the bank have the largest Θ_{max} (Figures 4g and 4h), with the very lowest Θ_{max} values occurring right over the center of the bank itself (210 and 410 km along the baseline in Figures 4g and 4h respectively).

To elucidate the source of this spatial variability, the gridded SSH, geostrophic velocity vectors, and glider Θ_{max} are displayed in Figure 5. The tendency toward higher Θ_{max} on the northern side of the bank is evident in the glider sections, though, as intimated above, there is also a suggestion that some warmer water (though with reduced Θ_{max}) is found against the southern side of the bank in the southwestern glider sections. The SSH and velocities help to explain this pattern. The region of elevated SSH on the northern side of the bank, extending from a meander of the ACC to the north, is consistent with ACC waters circulating around the deep basin to the northwest of the bank (as shown with the velocity vectors), before the signal is eroded to the southwest of the bank, presumably due to mixing with ambient waters. Following the velocity vectors, there appears to be a particularly strong reduction in Θ_{max} between the 36°W and 34°W glider sections (as indicated by the red arrow in Figure 5), with the final evidence of highly diluted warmer water being found at the southernmost tip of glider section 1 over the small detached seamount to the southeast (as denoted by the red-edged star).

The SSH-derived velocity vectors also confirm the anticyclonic circulation over the bank, as observed by Meredith et al. (2015). A small region of higher SSH is also observed around the northeastern tip of the bank—the source of this higher SSH water is less clear but may be related to the southward meander of the ACC due north of this location. It thus appears that waters of higher Θ_{max} are sourced from the ACC to the north before being modified as they encounter the anticyclonic circulation of the bank. This circulation is now discussed in more detail.

3.2. Circulation

While we should not necessarily interpret the float trajectories as entirely Lagrangian or representative of flow vectors at any particular depth, the pathways of both floats (Figure 2) indicate an anticyclonic flow over the bank. After deployment, float 8136 moves quickly toward the southwestern end of the bank, running roughly parallel to the topography, before moving along the southern side of the bank and then moving northwards to cross the bank around midway along its axis, before returning west again. Float 8135 moves northeastwards from its original position and completes an anticyclonic loop of the northeastern part of the bank during its 4-month deployment. However, in addition to the general anticyclonic vorticity observed, both floats have smaller loops present along their trajectories. These are best revealed by the higher temporal frequency sampling of float 8136. A series of subinertial cyclonic and anticyclonic loops can be seen both at the far southwestern end of the bank, and in a

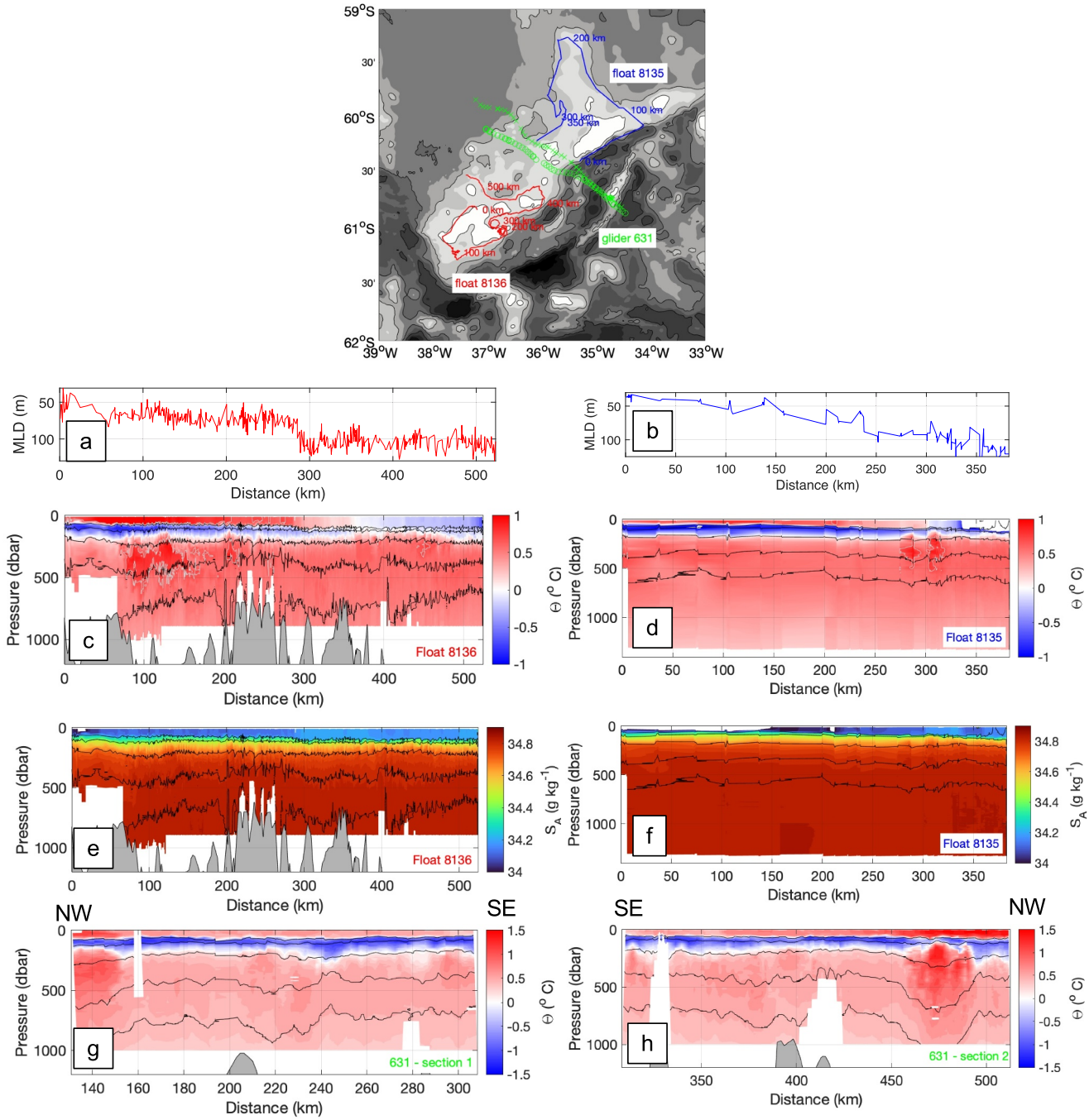

Figure 4. (a, b) Mixed layer depth (MLD) calculated using the de Boyer Montégut (2004) method of 0.03 kg m^{-3} above 10 m potential density, plotted by deployment distance for float 8136 and 8135 respectively. (c–f) Conservative temperature (with the 0.6°C isotherm in gray) and absolute salinity plotted by deployment distance for float 8136 and 8135 respectively. (g, h) Conservative temperature for glider sections 1 and 2 across Discovery Bank (immediately after the start of the deployment), with direction of transect indicated. Inset map shows location and distances along baseline of the two float trajectories, alongside the two glider sections (green circles = Section 1, green crosses = Section 2). γ_n surfaces 27.6, 27.8, 28, 28.1 and 28.15 kg m^{-3} (top to bottom) and GEBCO_2014 bathymetry are shown.

region of highly curved topography around 61°S 36.75°W. A further partial loop is seen around 59.9°S 35.8°W in float 8135, though the resolution of this feature is less clearly resolved owing to its 5-day sampling frequency.

The LADCP data allow us to understand more clearly the depth structure of the circulation. Figures 6a–6c shows the mean velocity vectors at the near-surface, mid-water column and near the bottom. In Meredith et al. (2015), it was argued that the anticyclonic Taylor column circulation extended from the ocean floor up to 300 m depth; the

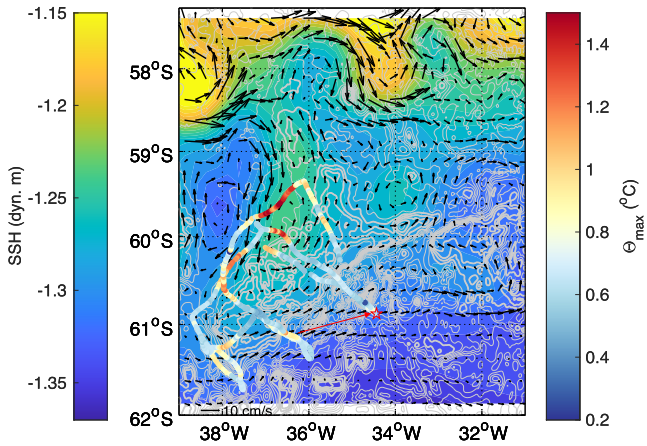

Figure 5. Mean AVISO SSH (in dynamic meters) for the period of the 631 glider deployment (2 February–9 April 2019) with mean geostrophic velocities (in cm s^{-1}) and CDW Θ_{max} (in °C) for the entire glider deployment. A 10 cm s^{-1} arrow is shown at the bottom of the plot as a key, and GEBCO_2014 bathymetry is included as light gray contours for orientation. The red arrow denotes the particularly large reduction in CDW temperature between the two glider sections, and the offshore movement of that core relative to the main part of Discovery Bank (red-edged star).

depth-averaged velocities in Figures 6a–6c largely accord with this. While there are clearly deviations from a smooth flow around the bank, most likely due to inertial motions in the near-surface layers and interaction with fine-scale topography near the bottom, the anticyclonic vorticity is seen strongly at all levels, with speeds typically between 10 and 20 cm s^{-1}. This result is confirmed by the data from float 8136 (Figure 6d), which typically show current speeds of 5–15 cm s^{-1} at all depths along the track of the vehicle. Similar anticyclonic circulation is seen from the glider depth-averaged velocities (0–1,000 m or the bottom if shallower), where there is further evidence of the very warmest CDW temperatures (Figure 5) coinciding with the strongest advection from the north (Figure 6f). In general, the strongest flows around the bank appear around the 3,000 m contour, with more mixed and weaker flows over the bank itself.

In addition to this general anticyclonic flow pattern, there is evidence from float 8136 of enhanced current speeds, particularly close to the bottom, as the float passes through the region of closed loops, with speeds reaching up to 30 cm s^{-1} as the float passes over this region of shallower bathymetry (Figure 6d). Similar but less pronounced enhancements of current speed are seen at the southwest corner of the bank and as the float passes over the ridge close to the end of the deployment. In each instance, there is significant vertical movement of the near bottom isopycnal ($\gamma^n = 28.1$ kg m^{-3}) between individual profiles and also a clear enhancement in vertical shear in the bottom 300 m compared with the other profiles (Figure 6e). Such elevated shear and strain is suggestive of enhanced near-bottom mixing; this is quantified explicitly in Section 4.

Inspection of the glider depth-averaged velocities and hydrographic sections yield further insights into the anticyclonic circulation. Meredith et al. (2015) previously highlighted opposing velocities on either side of the bank coinciding with the plunging of isopycnals toward the core of the bank itself. The glider depth-averaged velocities for Sections 1, 2, 7 and 8 (Figure 6f) clearly illustrate the differing flow direction between the two sides of the bank, but the glider temperature sections (Figures 4g and 4h) reveal a more complicated density structure, with some of the sections showing an uplift of the near-bottom isopycnals over the crest of the bank itself (see $\gamma^n = 28.1$ kg m^{-3} in Figure 4h at 410 km along the baseline). This is similar to the uplift seen in float 8136 as the float moves over shallower topography (Figure 4e), a detail which could not previously be resolved with ship-based CTD sections.

The mixing associated with the straining of isopycnals and shearing of the flow over the topography is discussed in Section 4.

4. Mixing and Heat Fluxes Over the Bank

4.1. Turbulent Kinetic Energy Dissipation Rates

Rates of turbulent kinetic energy dissipation (ε) and turbulent diffusivity (κ), derived from the finescale parameterization, are shown in Figures 7a and 7b. Data are not present in the top 100 m of the water column because of the moving window used and the need for a suitable segment length over which to evaluate the shear and strain.

A number of features can be distinguished from these plots. Firstly, background rates of dissipation away from the bottom boundary are generally low, O (10^{-10} W kg^{-1}), similar to typical open ocean values. However, dissipation in the bottom 200 m of many profiles is generally enhanced up to O (10^{-9} W kg^{-1}), and in the regions of the subinertial loops and where the float crosses the mid-point of the ridge, values of O (10^{-8} to 10^{-7} W kg^{-1}) are observed, with enhanced dissipation values extending from the sea floor up to 100 m depth (the upper limit of the mixing estimates). There is also a more general enhancement of dissipation in the top 300 m of the water column, likely associated with wind-driven mixing from the surface. The associated turbulent diffusivity κ (Figure 7b) increases from O (10^{-5} m^2 s^{-1}) to as high as O (10^{-2} m^2 s^{-1}) in the region of closed loops immediately above the topography.

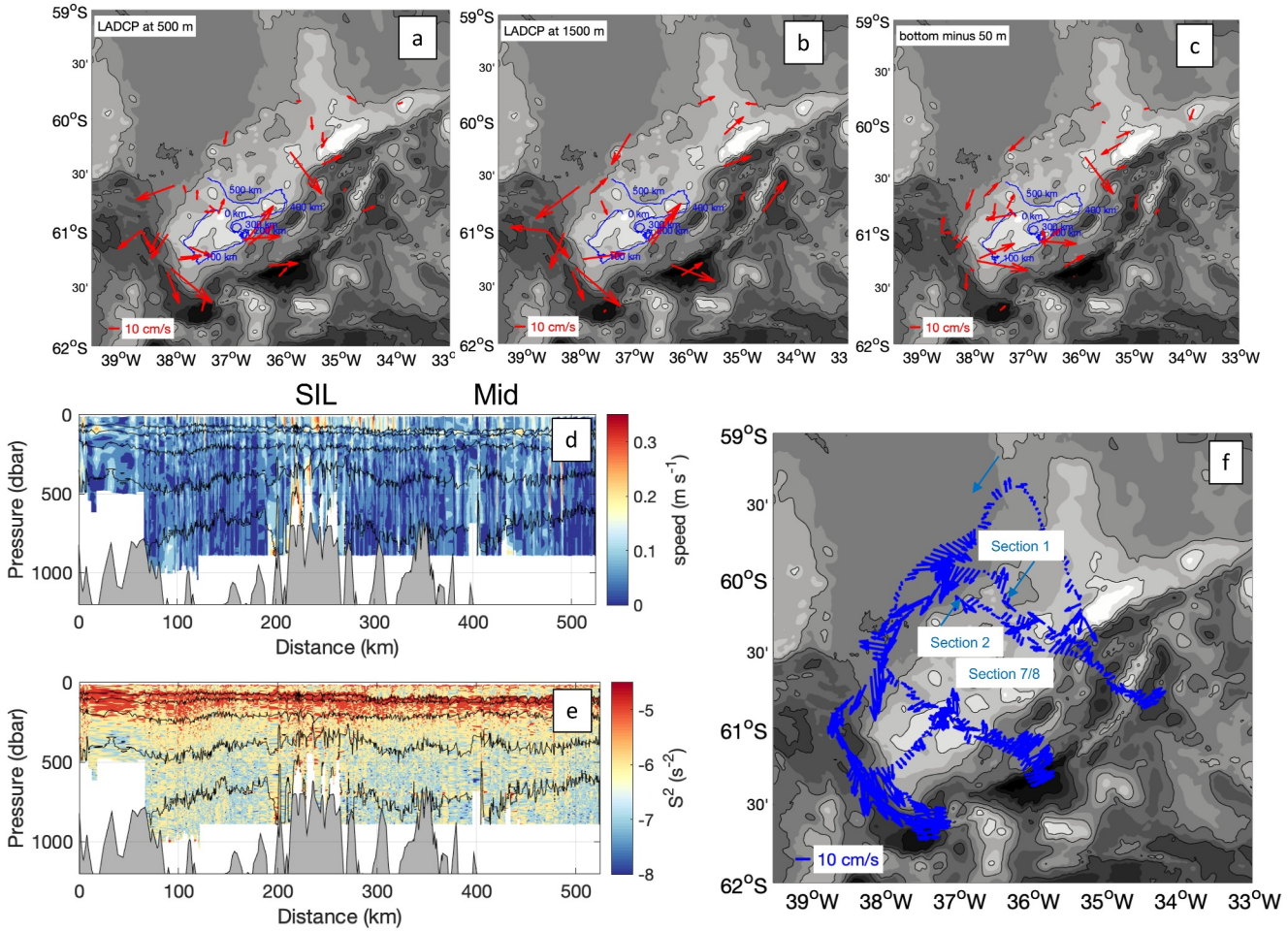

Figure 6. (a–c) Horizontal velocity vectors at 500, 1,500 m and mean of the bottom 50 m from the LADCP stations, with bathymetry as in Figure 2 shown. The path of float 8136 with distances every 100 km is marked; (d) Current speed from EM-APEX float 8136 and (e) vertical shear-squared, with γ_n surfaces at 27.6, 27.8, 28, 28.1 and 28.15 kg m^{-3} shown. The position of the subinertial loops (SIL) and where the float crosses the midpoint of Discovery Bank (Mid) is shown; (f) Depth-averaged velocities (0–1,000 m, or the bottom if shallower than 1,000 m) from glider 631, with sections referred to in the text marked.

The shear-to-strain ratio R_ω (Figure 7c) indicates the dominant frequency content of the internal wave field. Low values of R_ω indicate a high-frequency internal wave field (approaching N) dominated by vertical motions, while high values of R_ω indicate low-frequency internal waves (approaching f) with a preponderance of horizontal motions. Much of the water column has R_ω close to 5, but there is a general reduction with depth down to 3 (similar to GM) at 800 m. Particularly low values (1–2) are observed in the region of the closed loops. This is indicative of a high-frequency (approaching N) internal wave field, with a greater contribution to finescale variance from vertical motions. The apparent spike to higher values below 900 m is likely an artifact due to the very low number of data points going into the estimate (see error bars on Figure 7c, right).

The rotary coefficient (Figure 7d) shows there is a general dominance of CW-polarized energy along the path of the float, as evidenced by the greater prevalence of negative rotary coefficient values. This indicates a tendency for upward propagating energy over the Bank, as one may expect for internal wave energy generated at the bottom. There is no evidence for particular enhancement of these negative values in the region of the closed loops.

The enhancement of mixing in certain locations over the bank is confirmed by the individual microstructure profiles (Figure 8). While most of the stations have open ocean background ε values of O (10^{-11} to 10^{-10} W kg^{-1}), there are stations which have notably higher mean values. Stations 34 and 36, close to the region of the enhanced current speeds and closed loops, exhibit enhanced dissipation rates throughout the water column, with full-depth average values reaching 10^{-9} W kg^{-1}. Similarly, stations 26 and 37, located along the topography

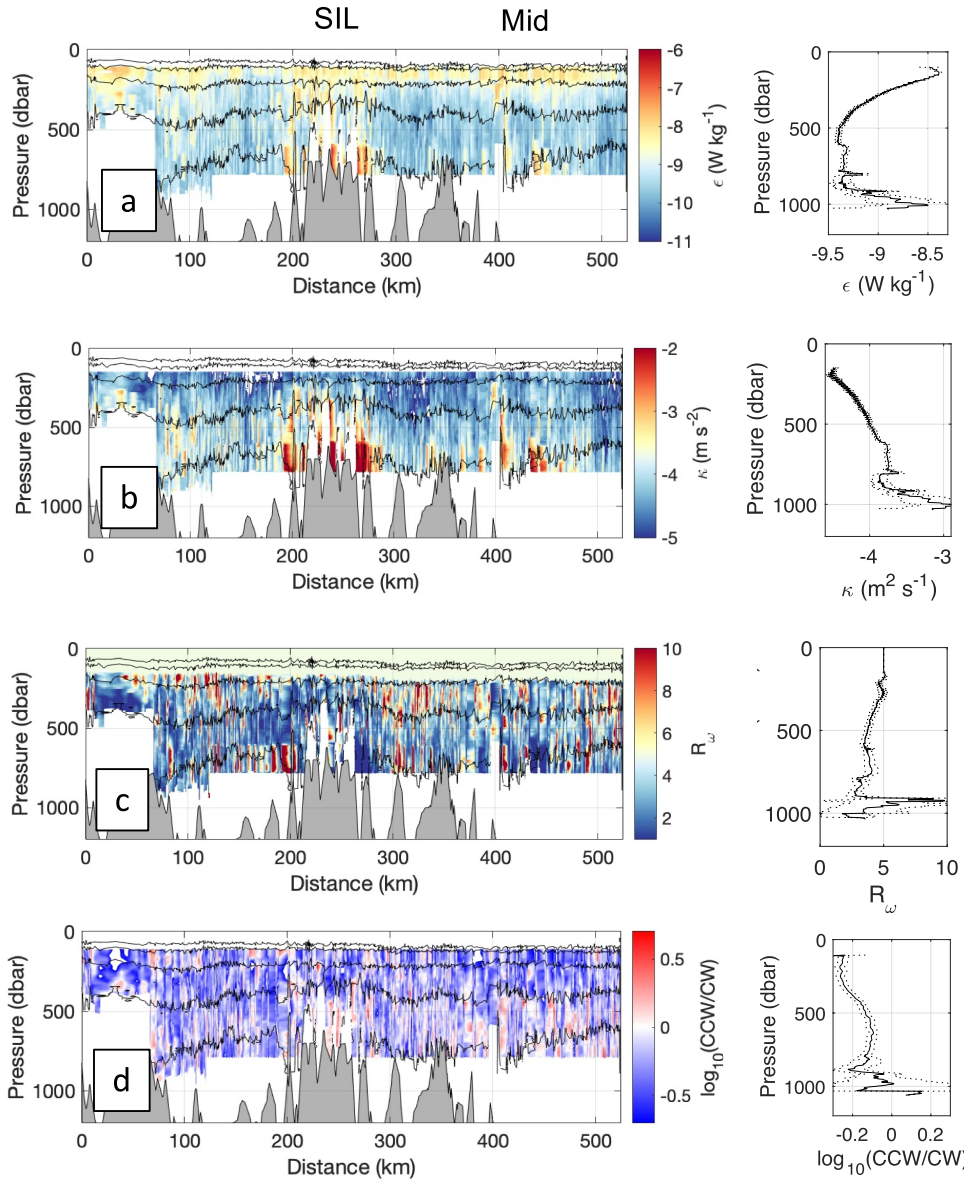

Figure 7. Sections and deployment mean (a) ε (W kg^{-1}); (b) κ (m^{2}s^{-1}); (c) R_ω and (d) log$_{10}$ (rotary coefficient) for float 8136, with bathymetry as in Figure 4. The dotted lines on the right hand panels represent the 2 standard error confidence interval on the mean. "SIL" and "Mid" show the locations of the subinertial loops and the position where the float crosses the midpoint of Discovery Bank.

in the northeast and southwest of the bank respectively, exhibit very strong dissipation rates throughout the water column, with particular enhancement in the bottom 200 m. Similar enhanced dissipation is also found at Station 24, on the southern edge of a small detached seamount off the southern side of Discovery Bank. It is thus clear from both the microstructure and finestructure measurements that many of the steeply sloping regions of the bank have strongly enhanced dissipation rates, which are magnified further in the bottom 200 m.

4.2. Heat Fluxes and Water Mass Property Variability

As previously observed, a key difference between the stations north of the array and those to the south and over the core of the bank is the erosion of the Θ_{max} (Figure 5). Meredith et al. (2015) previously posited that the water mass modification within the confluence occurred largely through water being retained for long periods during which it is slowly mixed, while Whitworth et al. (1994) argued, through *T/S* calculations, that it was the mixing of

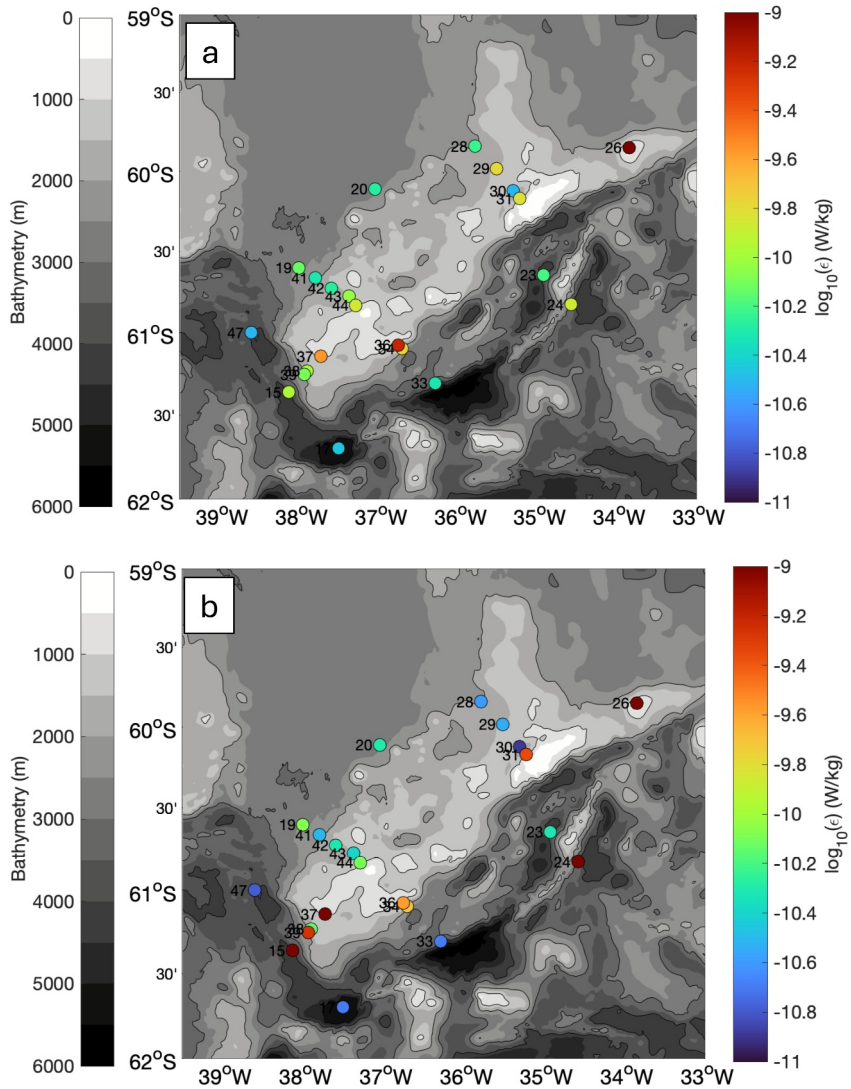

Figure 8. (a) Mean full depth ε (W kg^{-1}) for each of the Discovery Bank microstructure stations; (b), as (a), but confined to the bottom 200 m of the profile only. Bathymetry from GEBCO_2014 is contoured.

waters from the Weddell Sea and ACC, together with shelf waters derived from the Peninsula, that were responsible for the mid-depth minimum in stratification in the confluence. Here we argue that turbulent vertical mixing at "hotspots" over the ridge is also involved in these water mass transformations.

One way of understanding the processes occurring is by considering the mid-depth temperature structure, vertical heat flux, and position of the 0.6°C isotherm along the trajectory of float 8136 (Figure 9a). The rapid erosion of the $\Theta_{max,}$ seen between 100 and 275 km along the track (Figure 4a), and coinciding with the movement of the float along the southern side of the bank and into the region of closed loops, is clearly visible. Between 150 and 200 km, the temperature maximum separates into two cores, one centered around 300 m depth and another around 500 m. The strong temperature gradients generated, in conjunction with the enhanced diffusivity as the float approaches the shallow topography, leads to significantly enhanced heat fluxes on the upper and lower boundary of the isotherm (heat flux values are typically enhanced from ~0.5 to 3 Wm^{-2} in a band around 450–500 m, and from −0.5 to 2 Wm^{-2} in a band around 300–400 m).

Alongside this enhancement in mixing is a change in the Θ-S properties of the lower part of the water column (generally below 150 m) over the region of shallower topography (Figure 9b). The modified water mass encountered as the flow passes over the topography (with reduced Θ_{max} and denoted with a square in Figure 9b)

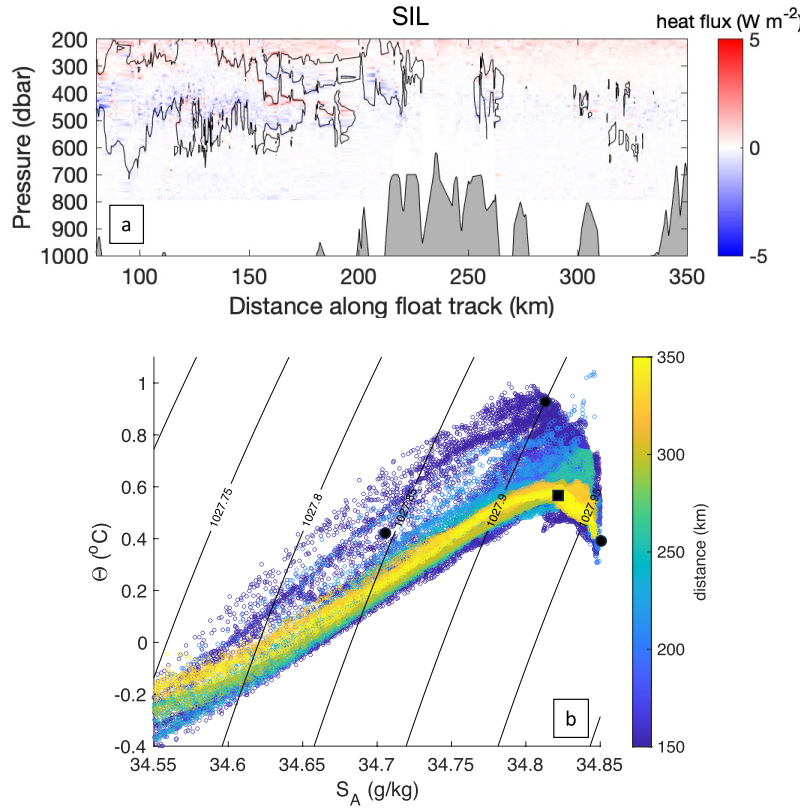

Figure 9. (a): Vertical heat fluxes (positive upwards) derived from the float CTD and finescale mixing estimates (scale in color). The 0.6°C isotherm is denoted with the solid contour, and the bottom topography from GEBCO_2014 and the position of the subinertial loops (SIL) is indicated; (b) Change in lower water column (>∼150 m) Θ-S properties for the same geographical domain, indicating that the modified Θ_{max} water (black square) can be generated from an admixture of unmodified Θ_{max} water seen in the earlier profiles, and cooler water masses above and below (black circles). Θ-S curves are colored by distance along the baseline (in km), and potential density contours referenced to the surface (in kg m^{-3}) are shown.

can clearly be generated through an admixture of the Θ_{max} water from earlier in the float's trajectory (before the flow encounters the shallower topography), with cooler waters from above and below the Θ_{max} (all denoted with black circles). Furthermore, there is clear evidence of rapid water column homogenization as the float passes over this region of shallower topography. Two clear examples of this are shown in Figure 10. Figure 10a shows the along-path stratification between a number of γ^n surfaces below ∼200 m depth. For the deeper layers (especially γ^n = 28.12–28.13 kg m^{-3}), large profile-to-profile variability in stratification occurs over the region of closed loops (centered on 230 km along the baseline), followed by a rapid reduction in stratification in the later profiles. For the deepest layer shown (typically between 480 and 540 m), this produces the lowest stratification along the entire float pathway.

Further detail of this difference in water mass properties is obtained by considering how Θ varies on γ_n surfaces (Figure 10b). Where the temperature varies significantly on isopycnals between individual profiles, stirring by eddies is assumed to be dominant, while homogeneity of temperature between profiles indicates a relatively pure well-mixed water mass. Meredith et al. (2015) previously observed that isopycnal stirring around the Taylor column was relatively high, with a horizontal diffusivity of 1,000–1,800 m^2 s^{-1} bringing surrounding waters from north and south of the bank into the Taylor column. Figure 10b shows that this resultant high interprofile temperature variability in the CDW inflow is strongly reduced as the float traverses from the southwest of the bank into the region of (and to the east of) the region of enclosed loops. Particularly homogenous water masses are observed downstream of 230 km along the baseline. Representative standard deviations at the γ^n = 28.13 kg m^{-3} level for 50–230 km along the baseline and 230–350 km along the baseline give values of 0.055°C and 0.033°C respectively. Further discussion of how to interpret this change in properties is given in Section 4.3, but it is clear

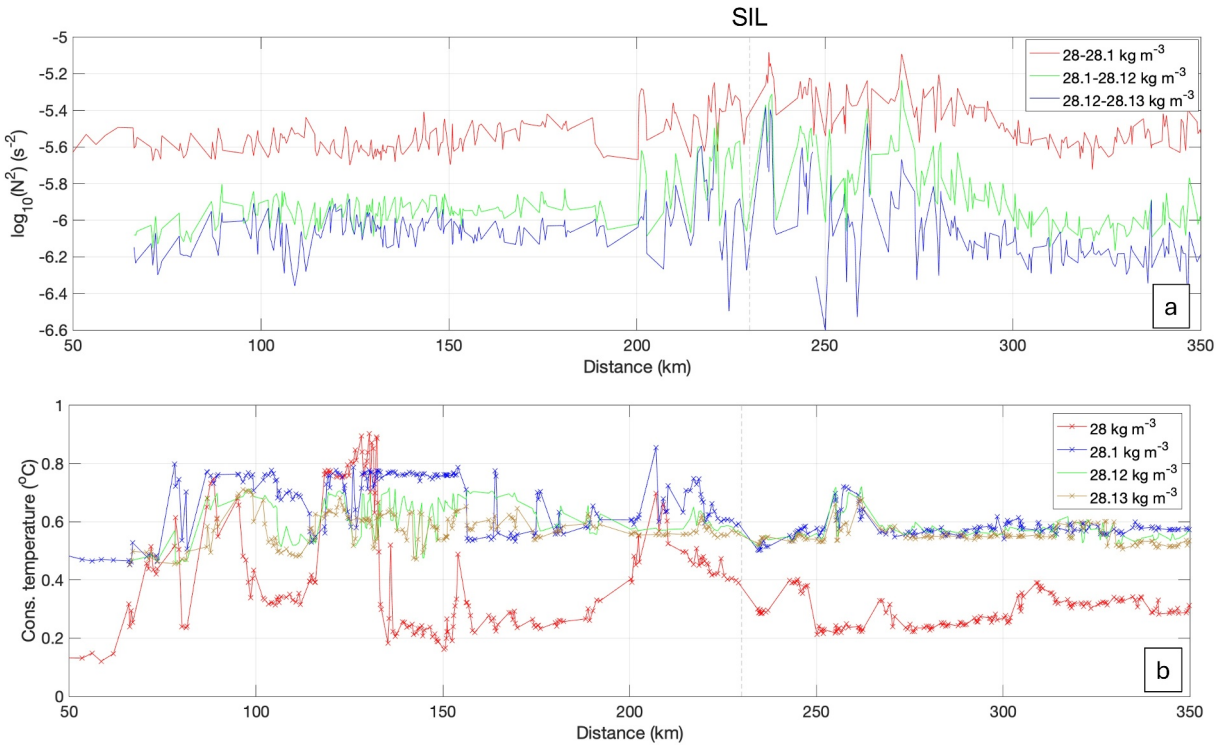

Figure 10. (a) Mean N^2 in a variety of neutral density layers for float 8136, plotted against distance along track. The location of the subinertial loops is marked 230 km along the baseline. (b) Conservative temperature Θ on a variety of neutral density surfaces. The mean depth of those surfaces is: 28 kg m^{-3} = 210 m, 28.1 kg m^{-3} = 393 m, 28.12 kg m^{-3} = 473 m, 28.13 kg m^{-3} = 530 m.

that the bank is host to water masses of highly differing stratification and properties over short horizontal distances, with turbulent mixing likely playing a key role in homogenization of these mid-depth (200–600 m) water masses (Figure 10b).

Further insights into where enhanced mixing and heat fluxes occur over the bank can be obtained from the CTD and microstructure data. For each profile, the mean upward heat flux between the CDW and WW layer (defined by the Θ_{max} and Θ_{min} below the mixed layer at each station), and the mean downward heat flux between the CDW layer and the bottom, is computed from the microstructure and CTD data using:

$$Q_{CDW\_WW} = -\rho c_p \kappa \frac{\partial \Theta_{CDW\_WW}}{\partial z} \tag{7}$$

and

$$Q_{BTM\_CDW} = -\rho c_p \kappa \frac{\partial \Theta_{BTM\_CDW}}{\partial z} \tag{8}$$

This method thus estimates the two-directional vertical heat flux out of the CDW layer.

The mean fluxes out of the CDW layer derived from the microstructure are displayed in Figure 11. While the mean upward fluxes from the CDW to the WW layer (Figure 11a) do not typically exceed 1 W m^{-2}, we observe that stations 24, 26, 34, 37 and 39 all have values exceeding 2 W m^{-2}. Station 34 is close to the location of the looped float trajectory, while stations 37 and 39 are located in the southwest corner of the bank, close to where the rapid transformation of CDW properties begins. Stations 24 and 26 (in the northeast corner of the bank and over a detached seamount) have particularly strong fluxes (over 6 Wm^{-2}); each of these locations are also over strongly sloping topography. Fluxes between the CDW and the bottom are much smaller (typically around 0.2 W m^{-2}), but these are again enhanced, particularly at stations 26, 29, 34 and 39 (values are between 1 and 2 W m^{-2}). This

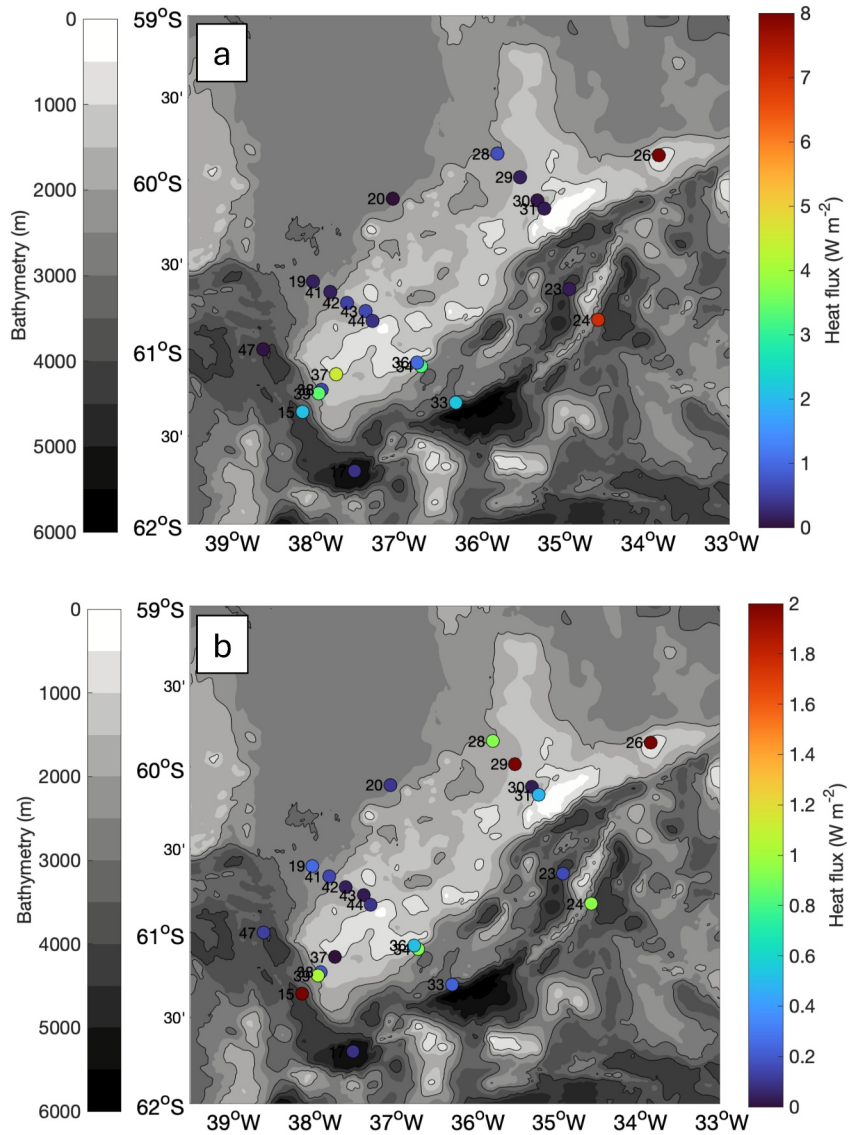

Figure 11. Mean vertical heat fluxes (a) out of the CDW layer upwards into the WW (positive upwards), or (b) downwards to the bottom of each profile (positive downwards), derived from the CTD and microstructure profiles, with bathymetry displayed as in Figure 8.

analysis thus confirms the earlier supposition that certain parts of the bank, particularly the steeply-sloping southern flank, exhibit strongly enhanced dissipation and heat fluxes compared to background values.

4.3. Water Mass Transformation

While a spatial coincidence between enhanced vertical heat flux and changes in mid-depth water mass properties has been demonstrated, a key question is whether the observed values of Q are sufficient in themselves to sustain the transformation in properties seen along the float path. This is important to the interpretation as the float trajectories themselves are not necessarily strictly representative of the dominant flow, with an indication from Figures 5 and 6f that the float track along the southern side of the bank does not necessarily follow the main flow direction in the vicinity of the subinertial loops (red arrow in Figure 5), as discussed in Section 3.1. This may mean that differences in water mass properties observed in Figure 10 reflect spatial as well as temporal changes to a level not fully established, with the float moving more onshore relative to the bank (i.e., away from the CDW core on the southern side of the bank and into the core of the Taylor column).

To quantify the direct impact of vertical mixing observed by the float passing over the region of shallow topography, we consider the following simple 1D temperature budget:

$$\frac{D\overline{T}}{Dt} = \frac{Q_+ - Q_-}{\rho_0 c_p \Delta z} \tag{9}$$

where $\overline{T}$ is the mean temperature of the layer greater than 0.6°C, $Q_+ - Q_-$ is the total heat flux out of the layer and Δz is the thickness of the layer. The left-hand term can be directly evaluated by calculating the mean layer-averaged temperature and time separation (40 days) from 75 to 175 km along the baseline (before the flow encounters the region of the subinertial loops) and 300–400 km along the baseline (after the flow has passed this region). The right-hand term is approximated from the microstructure data in Figure 11 by calculating the mean vertical heat flux divergence from Stations 34 and 36, closest to the subinertial loops, estimated at 2.11 W m^{-2}. Δz is the mean layer thickness before the transformation (354 m). The left-hand side of the equation evaluates to $\sim 2 \times 10^{-6}$ °C s^{-1}, while the right-hand side is much lower, at $\sim 1.6 \times 10^{-9}$ °C s^{-1}.

It is thus clear from this calculation that the accumulated vertical heat flux over the 40 days is not sufficient on its own to produce the water mass transformation of the layer observed. There are a several possible reasons for the large discrepancy. The first is that the equation itself is 1D in form, but horizontal fluxes of temperature will also likely strongly affect the heat budget of the region. Second, there is the assumption that both the temperature structure and heat fluxes at any point are constant in time; we lack the observations to test this robustly. Third, the more likely interpretation of the float trajectory is that it has moved from the region of CDW inflow on the southern side of the bank (Figure 5) into the middle of the Taylor column itself, where it is postulated that water can be retained for much longer periods, possibly up to several years (Meredith et al., 2015). It is over this timescale that the diapycnal mixing processes may act, as opposed to the 40-day timescale of the single direct float pathway. It was shown in Figure 8, and is discussed further in Section 5, that zones of high mixing are likely widespread over many steeply sloping areas on the southern side of the bank, suggesting that diapycnal transformation is important for waters retained within the column.

In addition, we observe that the sharp curvature of the topography in the closed loop region may form a preferential pathway for water external to the column (in this case warmer CDW) to intrude into the center of the Taylor cap, helping to account for the relatively high isopycnal mixing rates of 1,000–1,800 m^2 s^{-1} observed in Meredith et al. (2015). A similar transition in water mass properties from the float data, this time from the center of the column to the CDW core, is seen around 80 km along the baseline on the western end of the bank (Figure 4c), again at a sharp curvature in the topography (Figure 4, top panel). A complete quantitative analysis of all isopycnal and diapycnal transformation processes would require a far greater density of float and microstructure observations than were obtainable within this study. However, these observations show that the combination of a retentive stratified Taylor column circulation directing CDW from the north anticyclonically around the bank, localized hotspots of vertical mixing in the region, and the exchange of water masses between the edge and core of the column all need to be quantified to understand fully the frontal dynamics of the Weddell Front and the Confluence.

5. Mechanisms of Vertical Mixing

It is clear from the above analysis that mixing is enhanced over the steeply sloping topography of the bank, vigorously mixing water retained within the Taylor column. The most likely candidate mechanism to explain such an enhancement of mixing is the generation of shear through internal tide generation as barotropic tides flow over the shallow topography. In this section, we quantify both the barotropic tidal velocities over Discovery Bank and the depth-integrated barotropic to baroclinic conversion rates, to understand whether our observed spatial variability in ε and Q is consistent with this mechanism.

5.1. Barotropic Tides

Maps of model-derived barotropic tidal velocity over Discovery Bank (Section 2.7) show that, while overall barotopic tidal speeds are weak (typically 3–6 cm s^{-1}), shallow regions on the southern flank of the bank exhibit much higher tidal velocities, up to 15 cm s^{-1} in the region of the closed loops and over 20 cm s^{-1} over the shallow bank further northeast (Figure 12a). Inspecting the main tidal constituents separately, the region of the closed

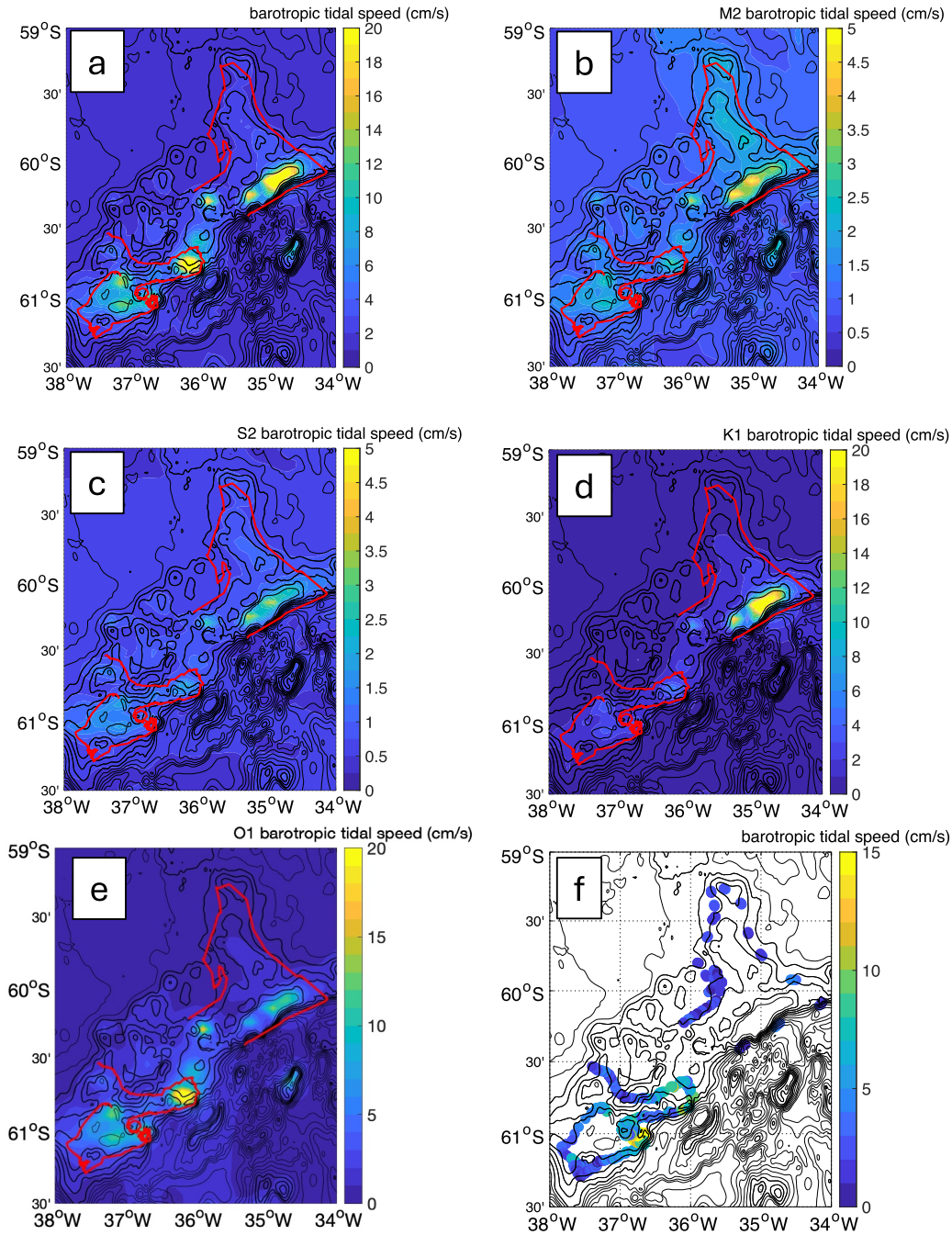

Figure 12. (a) Mean barotropic tidal speed (all components) for the period of float 8136's deployment given in Table 1. Bathymetry from GEBCO_2014 is shown at 500 m intervals, with 500, 1,000 and 1,500 m contours shown in bold, and float trajectories in red; (b) As (a) but for M2 only (note different color bars) (c) S2; (d) K1; (e) O1; (f) Mean tidal speed at time of individual float profiles for both floats.

loops has mean tidal speeds of 1.8 cm s^{-1} for M2, 1.4 cm s^{-1} for S2, 3.9 cm s^{-1} for K1 and 14.1 cm s^{-1} for O1 (Figures 12b–12e). Individual time series of area-averaged mean tidal speeds (not shown) also reveal a significant spring-neap variability, with area-averaged speeds for all constituents combined varying between 1.5 and 4.1 cm s^{-1}.

While the region of closed loops is certainly an area of enhanced tidal velocities, Figure 12 does not suggest it has uniquely high barotropic tidal speeds over the bank, with many of the shallow regions both to the southwest and

northeast having equivalent or higher mean speeds. However, by extracting the dominant tidal constituents at the time the individual EM-APEX profiles were collected (Figure 12f), it is apparent that the period the float occupied the region of the closed loops was a spring period of particularly strong velocities (late March 2019), with barotropic speeds of up to 20 cm s^{-1}, while those areas in the southwest of the bank and northeast with equivalently strong tidal flows were occupied at neap tide, and thus the float only encountered velocities of 2–6 cm s^{-1} there. This likely explains the very high mixing rates calculated from the finescale float data in that particular region.

5.2. Barotropic to Baroclinic Conversion Rates

The overlap between the regions of most vigorous turbulent mixing and the strongest tidal velocities (mostly controlled by O1 and K1) is striking, and strongly suggestive that the generation of internal tides is responsible for the observed mixing and water mass changes documented above. To investigate this further, we quantified the internal tidal forcing using the method of Sherwin (1988). This technique uses a combination of the tidal velocities estimated in Section 5.1 alongside the bathymetry and stratification data to estimate an internal tidal forcing function F:

$$F = \frac{i\,z\,L\,N^2}{\omega}\nabla\left(\frac{1}{H}\right) \tag{10}$$

where L is the tidal flow (defined as uH, vH where u and v are the eastward and northward velocities and H is the water depth), ω is the frequency of the internal tide and $\nabla\left(\frac{1}{H}\right)$ is the horizontal gradient of the inverse of the water depth. The depth profile of N^2 is obtained from a mean of all the CTD profiles in the survey (Figure 2), and individual estimates of F are calculated for M2, S2, K1 and O1 tidal frequencies respectively. The depth-integrated forcing function F^* is then calculated at each point in the domain as:

$$F^* = \int \rho F\,dz \tag{11}$$

Maps of F^* for each component (Figure 13) reveal that conversion rates are typically low (spatial mean values for M2, S2, K1 and O1 are 2.94, 1.74, 5.80 and 9.00 N m^{-2} respectively), but that values are strongly enhanced over the steeply sloping parts of the bank, especially on the southern flank. For M2 and S2, values on the southern flank of the bank reach 20–40 N m^{-2}, while for K1 and O1 values of up to 150–200 N m^{-2} are observed, notably over the northeastern corner of the bank, in the region of the closed subinertial loops, and over the detached seamount to the south of DB. Recalling Section 4.2, each of these sites were locations of the strongest dissipation and heat fluxes over the bank.

It is notable that the strongest internal tide generation occurs at diurnal frequencies, which is a lower frequency than the inertial frequency f, at this latitude being 1.26×10^{-4} s^{-1}, or 13.8 hr. These internal tidal motions thus do not directly force the internal wave band (between f and N), and theory predicts that these evanescent waves decay exponentially away from the source. Determining the exact pathway between these bottom-trapped waves, the internal wave shear observed by the EM-APEX float and turbulent mixing is not possible from our data, but several possible mechanisms have been proposed. The nonlinear terms in the equation for the conversion of barotropic to baroclinic wave energy may contribute to tidal energy conversion through tide-topography interaction (Bell, 1975; Nakamura et al., 2000), with Dale et al. (2001) arguing that these processes may produce topographically-trapped baroclinic wave-like motions. Furthermore, Vlasenko et al. (2005) showed that the advective term can lead to the generation of unsteady lee waves. Rippeth et al. (2017) also demonstrated in the Arctic that lee wave generation coupled with supercritical barotropic tidal flow over sloping topography is a key mechanism for the transfer of energy from the tide to turbulent mixing poleward of the critical latitude.

In contrast, M2 and S2 do fall within the internal wave band, meaning that despite their lower conversion rates, this may act as a more efficient mechanism for converting barotropic tidal kinetic energy into internal wave kinetic energy, which can then cascade to dissipative scales. The observed low R_ω approaching the bottom suggests a dominance of high-frequency waves (Figure 7c). A detailed study of the internal wave energetics cascade is beyond the scope of the study, as it would require fixed moorings to quantify the meridional and zonal

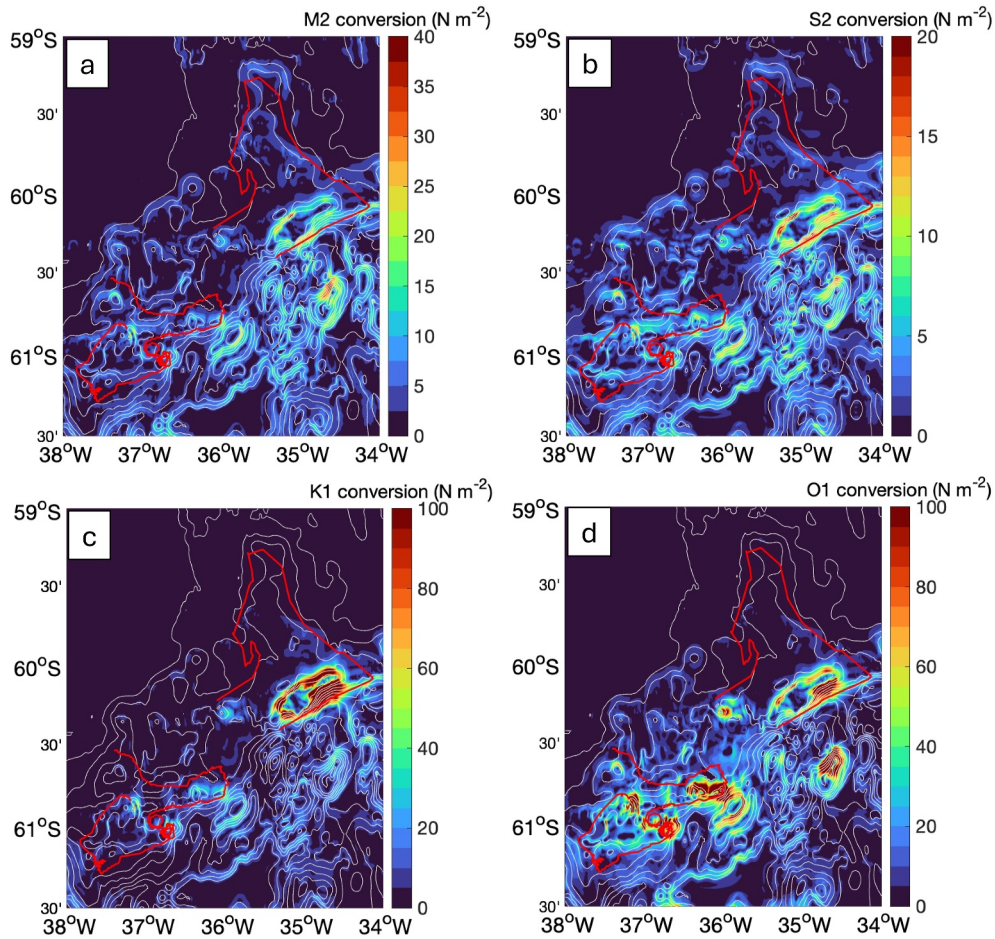

Figure 13. Barotropic to baroclinic conversion rates over Discovery Bank (in N m^{-2}) for the four main tidal components (a) M2; (b) S2; (c) K1; (d) O1. Bathymetry as in Figure 12 is plotted with white contours for orientation. Note different color bar limits for the different frequencies.

gradients in velocity, though other Southern Ocean studies over rough topography have illustrated the presence of a downscale cascade of energy from tidal (or geostrophic) motions, through internal waves and down to dissipative scales (e.g., Brearley et al., 2013; Cusack et al., 2020; Sheen et al., 2013).

5.3. Relationship With Taylor Column and Fate of Water

While the role of stratified Taylor column dynamics along the ridge had been previously established, we have demonstrated that strongly enhanced tidal-driven mixing over steep topographic slopes enhances heat fluxes significantly above background levels and, if acting on the same water mass for a long enough period, may contribute to the maintenance of the stratification minimum that is characteristic of the confluence. The circulation patterns observed by the ADCP, floats, altimetry and gliders confirm that the anticyclonic retentive properties of the flow observed by Meredith et al. (2015) are persistent in time, and a clear incorporation of warm CDW from the ACC into the column was observed (Figure 5).

While our observations are necessarily limited in time, a picture thus emerges of strong diapycnal mixing processes acting over steeply sloping parts of the bank, while the large-scale flow is retained for months to years. It is likely that some waters will make several loops of the ridge (as seen in Meredith et al. (2015)), entraining water from both the ACC and the Weddell Gyre to the south, while waters will sometimes short circuit the full loop of the bank moving from the periphery to the core of the Taylor column (as seen in float 8136). While our observations are limited, it appears that conversion into baroclinic shear is strongest at spring tides—thus the fastest

transformations are likely to occur at the locations where the strongest barotropic tides interact with the steepest topography, and be patchy in time (Figure 12f).

A detailed account of the downstream fate of the confluence waters requires further study, but Meredith et al. (2015) previously identified several seamounts conducive to Taylor column formation in the Scotia Sea. The degree to which each of these seamounts is the site of enhanced mixing is unclear, but the similar topographic forms and barotropic tidal speeds mean this is a likely outcome. The persistence of the minimum in stratification has been traced via unsupervised clustering techniques of hydrographic data around the edge of the Weddell Gyre (Jones et al., 2023). It thus seems likely that the combination of Taylor column retention alongside strong deep and mid-depth tidal mixing maintains a significant water mass class that can persist throughout much of the northern part of the Weddell Gyre south of the Southern Boundary of the ACC.

6. Conclusions

A detailed hydrographic, ADCP, EM-APEX float and glider study of Discovery Bank, in the Weddell Scotia Confluence, has yielded new insights into the pathways of mid-depth water masses on the South Scotia Ridge, and how waters from the ACC, Weddell Gyre and potentially the Antarctic Peninsula are retained and vigorously mixed over the steep topography of the ridge. The elevation of vertical heat fluxes (from 0.5 to 3 W m^{-2}) caused by this bottom-enhanced tidal mixing likely contributes to the homogenization of Θ on density surfaces, and the maintenance of low mid-depth stratification that is observed in the waters in the center of the Taylor column. Several sites of strong barotropic to baroclinic tidal energy conversion are observed on Discovery Bank, with finescale analysis of the float data implying an overall upward propagation of internal wave energy, and a preponderance for high-frequency internal waves to dominate particularly toward the bottom of the water column over the ridge.

There are a number of implications for these results. While the combination of the Taylor column circulation structure, long-timescale retention, and enhanced isopycnal mixing rates had been observed previously, the likelihood that many seamounts on the ridge host significantly enhanced diapycnal mixing and are sufficiently shallow that mid-depth CDW can be modified means that diapycnal mixing may play a key role in the maintenance of the mid-depth stratification minimum of the confluence. This is significant for the downstream evolution of the Weddell Gyre—it is known that the CDW from the ACC and confluence intrudes into the gyre at its eastern edge, eventually flowing toward the southwestern Weddell Sea where these water masses intrude onto continental shelves and mix with cold shelf waters—a process that, via brine rejection, ultimately leads to the production of AABW (Nicholls et al., 2009).

A further implication, though not directly the subject of this study, is the effect of the circulation on the biology and biogeochemistry of the surface layers, specifically the supply of the limiting micronutrient iron into the mixed layer. While the region of enhanced turbulent mixing can be seen in Figure 7a extending up to 200 m depth, and there are stations where these processes generate significantly enhanced heat fluxes (Figures 9 and 11), the direct impact on iron fluxes into the euphotic zone and resultant biological productivity is not properly understood. Previous studies have suggested several ways in which Taylor column dynamics may enhance productivity, including in the Indian Ocean sector of the Southern Ocean (Perissinotto & Duncombe Rae, 1990) and in the North Pacific (Dower et al., 1992). One may envisage that the combination of a highly-retentive circulation which encourages a build-up of nutrients, combined with vigorous turbulent mixing may enhance iron supply to the euphotic zone, but without direct biogeochemical measurements the relative effects of different sources cannot be isolated. There is also evidence that iron from the Peninsula is supplied from beneath the mixed layer into the Southern Boundary and across to Discovery Bank (Frants et al., 2013; Jiang et al., 2019)—whether the vertical mixing processes identified in this study are key to delivering this micronutrient to the euphotic zone is unclear. These questions will be the focus of future studies and will be key to further understanding the anomalously high production of the Scotia Sea region.

Finally, there is an increasing recognition that stratified Taylor Columns are prominent sites of diapycnal mixing across the Southern Ocean, in regions as diverse as the open ocean Scotia Sea (Balwada et al., 2016; Sévellec et al., 2015), Pine Bank to the west of OP (Prend et al., 2019), and Maud Rise (Mohrmann et al., 2022). While the individual mechanisms of diapycnal mixing appear different at each site (lee waves from geostrophic flows, enhanced vertical velocities, internal tides or thermobaric/double diffusive convection), we have demonstrated that

quantifying the combined effects of retention, frontal processes, isopycnal mixing and diapycnal processes is key to estimating accurately the modification of mid-depth and deep Southern Ocean water masses.

Appendix A: Details of Microstructure Processing

During the cruise, the VMP data were processed with ODAS Version 4.3 with standard parameters. This processing version includes the so-called "Goodman correction" (Goodman et al., 2006) to correct for contamination of the microscale shear measurements due to vibration of the instrument platform. In the context of an analysis of regional turbulence and mixing levels from a different region it was later found that the Goodman correction causes an apparent underestimation of dissipation in regions of weak turbulence when compared with data from the older High-Resolution Profiler (HRP) (Schmit et al., 1988), but that there is good agreement between the data collected with the two instruments when the VMP data are processed without the Goodman correction (Thurnherr et al., 2020). Ferron et al. (2023) argue that shear microstructure data collected with free falling instruments in regions of weak turbulence are contaminated by platform vibration that must be removed. Since vibration correction was not part of HRP processing this inference implies that the HRP measurements from regions of weak turbulence (Polzin et al., 1997) also do not reflect oceanic conditions but are dominated by instrument noise. It is not clear how this inference can be reconciled with the agreement of HRP-derived mixing estimates with those derived from tracer release experiments that has been reported before in regions of weak diapycnal mixing (Ledwell et al., 1993).

While Ferron et al. (2023) argue that correcting microscale shear measurements for instrument vibration is important, they also state that the correction published by Goodman et al. (2006) and implemented in ODAS Version 4.3 is in itself biased and requires an additional correction. This secondary bias correction is included in ODAS Version 4.5. There are, therefore, three different ways instrument vibration has been dealt with in published microstructure data: 1. Without correction; this includes all HRP data as far as we know, the DoMORE VMP data, and likely other older VMP data sets as well; 2. With the biased (uncorrected) Goodman correction; this includes all the data processed with ODAS Versions 4.3 (and possibly earlier) and 4.4; 3. With the bias-corrected Goodman correction; at present, this presumably only includes the data from Ferron et al. (2023) as well as the data from this manuscript. When applied to the Discovery Bank VMP data the results from the three treatments of vibration diverge for dissipation levels below about 10^{-9} W kg^{-1}, with the overall mean level differing by about factor 2.5 (Figure A1).

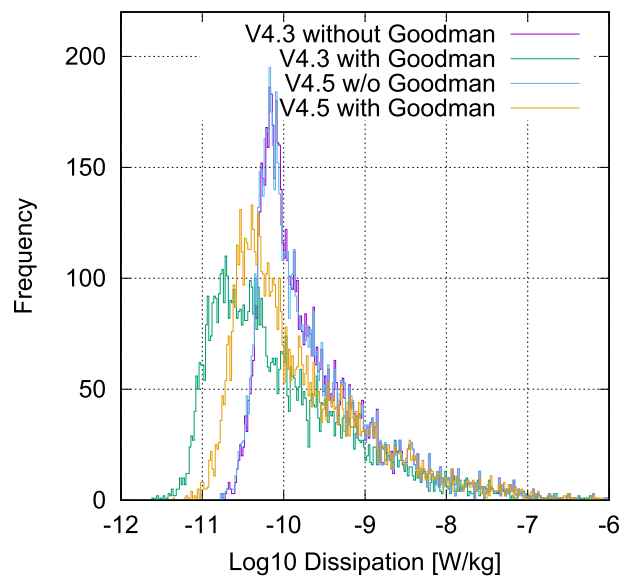

Figure A1. Distribution of dissipation resulting from processing the Discovery Bank VMP data with different methods for treating contamination due to instrument vibration. Blue and magenta: data processed without correcting for instrument vibration—mean dissipation of 2.4×10^{-10} W kg^{-1}; green: data processed with the vibration correction of Goodman et al. (2006)—mean dissipation of 1.0×10^{-10} W kg^{-1}; gold: data processed with the modified vibration correction of Goodman et al. (2006) as proposed by Ferron et al. (2023)—mean dissipation of 1.7×10^{-10} W kg^{-1}.

Data Availability Statement

The CTD, LADCP, float, glider and microstructure data are available online from BODC (Brearley, 2024; Brearley et al., 2024; Brearley & Girton, 2024; Thurnherr & Brearley, 2024; Thurnherr & Middleton, 2024). The altimeter products were produced by Ssalto/Duacs and distributed by Aviso, with support from CNES (2011) and can be found online (https://www.aviso.altimetry.fr/en/data/data-access/gridded-data-extraction-tool.html). The model fields for the tidal velocities are at https://www.esr.org/research/polar-tide-models/list-of-polar-tide-models/cats2008/.

Acknowledgments
We thank the officers and crew of RRS James Clark Ross for their support of the fieldwork during cruises JR18004 and JR18005, and also Hugh Fargher at Teledyne Webb Research for assistance in float setup. This work was supported by NERC Grants ORCHESTRA (NE/N018095/1) and ENCORE (NE/V013254/1) and by an Independent Research Fellowship (NE/L011166/1). This study has been conducted using E.U. Copernicus Marine Service Information for the AVISO altimetry data (Section 2.5).

References

Abrahamsen, E. P., Meijers, A. J. S., Polzin, K. L., Naveira Garabato, A. C., King, B. A., Firing, Y. L., et al. (2019). Stabilization of dense Antarctic water supply to the Atlantic Ocean overturning circulation. *Nature Climate Change*, *9*(10), 742–746. https://doi.org/10.1038/s41558-019-0561-2

Balwada, D., Speer, K. G., LaCasce, J. H., Owens, W. B., Marshall, J., & Ferrari, R. (2016). Circulation and stirring in the Southeast Pacific Ocean and the Scotia Sea sectors of the Antarctic circumpolar current. *Journal of Physical Oceanography*, *46*(7), 2005–2027. https://doi.org/10.1175/JPO-D-15-0207.1

Bell, T. H. (1975). Lee waves in stratified flows with simple harmonic time dependence. *Journal of Fluid Mechanics*, *67*(4), 705–722. https://doi.org/10.1017/S0022112075000560

Brearley, J. A. (2019). Cruise report - RRS James Clark Ross JR18004. Retrieved from https://www.bodc.ac.uk/data/information_and_inventories/cruise_inventory/report/jr18004.pdf

Brearley, J. A. (2024). Slocum underwater glider data for ORCHESTRA Discovery Bank deployment (Unit 631). https://doi.org/10.5285/1fbbf616-013c-76fc-e063-7086abc0a7d5

Brearley, J. A., Abrahamsen, E. P., & Bett, D. D. T. (2024). CTD cast data from the ORCHESTRA cruise JR18004 in the Scotia Sea. https://doi.org/10.5285/1fb82ba5-edf9-9e4d-e063-7086abc04a8e

Brearley, J. A., & Girton, J. B. (2024). EM-APEX float data from platforms 8135 and 8136 deployed from JR18004. https://doi.org/10.5285/1fbc6823-de6a-b38a-e063-7086abc03679

Brearley, J. A., Sheen, K. L., Garabato, A. C. N., Smeed, D. A., & Waterman, S. (2013). Eddy-induced modulation of turbulent dissipation over rough topography in the Southern Ocean. *Journal of Physical Oceanography*, *43*(11), 2288–2308. https://doi.org/10.1175/JPO-D-12-0222.1

Campbell, E. C., Wilson, E. A., Moore, G. W. K., Riser, S. C., Brayton, C. E., Mazloff, M. R., & Talley, L. D. (2019). Antarctic offshore polynyas linked to Southern Hemisphere climate anomalies. *Nature*, *570*(7761), 319–325. https://doi.org/10.1038/s41586-019-1294-0

Cusack, J. M., Brearley, J. A., Garabato, A. C. N., Smeed, D. A., Polzin, K. L., Velzeboer, N., & Shakespeare, C. J. (2020). Observed eddy–internal wave interactions in the Southern Ocean. *Journal of Physical Oceanography*, *50*(10), 3043–3062. https://doi.org/10.1175/JPO-D-20-0001.1

Dale, A. C., Huthnance, J. M., & Sherwin, T. J. (2001). Coastal-trapped waves and tides at near-inertial frequencies. *Journal of Physical Oceanography*, *31*(10), 2958–2970. https://doi.org/10.1175/1520-0485(2001)031<2958:CTWATA>2.0.CO;2

Davis, P. E. D., Jenkins, A., Nicholls, K. W., Dutrieux, P., Schröder, M., Janout, M. A., et al. (2022). Observations of modified warm deep water beneath Ronne ice shelf, Antarctica, from an autonomous underwater vehicle. *Journal of Geophysical Research: Oceans*, *127*(11), e2022JC019103. https://doi.org/10.1029/2022JC019103

de Boyer Montégut, C., Madec, G., Fischer, A. S., Lazar, A., & Iudicone, D. (2004). Mixed layer depth over the global ocean: An examination of profile data and a profile-based climatology. *Journal of Geophysical Research: Oceans*, *109*(C12). https://doi.org/10.1029/2004JC002378

Dower, J., Freeland, H., & Juniper, K. (1992). A strong biological response to oceanic flow past Cobb Seamount. *Deep-Sea Research, Part A: Oceanographic Research Papers*, *39*(7), 1139–1145. https://doi.org/10.1016/0198-0149(92)90061-W

Dufour, C. O., Griffies, S. M., de Souza, G. F., Frenger, I., Morrison, A. K., Palter, J. B., et al. (2015). Role of mesoscale eddies in cross-frontal transport of heat and biogeochemical tracers in the Southern Ocean. *Journal of Physical Oceanography*, *45*(12), 3057–3081. https://doi.org/10.1175/JPO-D-14-0240.1

Egbert, G. D., & Erofeeva, S. Y. (2002). Efficient inverse modeling of barotropic ocean tides. *Journal of Atmospheric and Oceanic Technology*, *19*(2), 183–204. https://doi.org/10.1175/1520-0426(2002)019<0183:EIMOBO>2.0.CO;2

Ferron, B., Aubertot, P. B., Cuypers, Y., & Vic, C. (2023). Removing biases in oceanic turbulent kinetic energy dissipation rate estimated from microstructure shear data. *Journal of Atmospheric and Oceanic Technology*, *40*(1), 129–139. https://doi.org/10.1175/JTECH-D-22-0035.1

Foppert, A., Donohue, K. A., Watts, D. R., & Tracey, K. L. (2017). Eddy heat flux across the Antarctic circumpolar current estimated from sea surface height standard deviation. *Journal of Geophysical Research: Oceans*, *122*(8), 6947–6964. https://doi.org/10.1002/2017JC012837

Frants, M., Gille, S. T., Hatta, M., Hiscock, W. T., Kahru, M., Measures, C. I., et al. (2013). Analysis of horizontal and vertical processes contributing to natural iron supply in the mixed layer in southern Drake Passage. *Deep Sea Research Part II: Topical Studies in Oceanography*, *90*, 68–76. https://doi.org/10.1016/j.dsr2.2012.06.001

Garrett, C., & Munk, W. (1975). Space-time scales of internal waves: A progress report. *Journal of Geophysical Research*, *80*(3), 291–297. https://doi.org/10.1029/JC080i003p00291

Goodman, L., Levine, E. R., & Lueck, R. G. (2006). On measuring the terms of the turbulent kinetic energy budget from an AUV. *Journal of Atmospheric and Oceanic Technology*, *23*(7), 977–990. https://doi.org/10.1175/JTECH1889.1

Gregg, M. C. (1989). Scaling turbulent dissipation in the thermocline. *Journal of Geophysical Research: Oceans*, *94*(C7), 9686–9698. https://doi.org/10.1029/JC094iC07p09686

Gregg, M. C., D'Asaro, E. A., Riley, J. J., & Kunze, E. (2018). Mixing efficiency in the ocean. *Annual Review of Marine Science*, *10*(1), 443–473. https://doi.org/10.1146/annurev-marine-121916-063643

Henyey, F. S., Wright, J., & Flatté, S. M. (1986). Energy and action flow through the internal wave field: An eikonal approach. *Journal of Geophysical Research: Oceans*, *91*(C7), 8487–8495. https://doi.org/10.1029/JC091iC07p08487

Heywood, K. J., Naveira Garabato, A. C., Stevens, D. P., & Muench, R. D. (2004). On the fate of the Antarctic slope front and the origin of the Weddell front. *Journal of Geophysical Research*, *109*(C6), C06021. https://doi.org/10.1029/2003JC002053

Huppert, H. E. (1975). Some remarks on the initiation of inertial Taylor columns. *Journal of Fluid Mechanics*, *67*(2), 397–412. https://doi.org/10.1017/S0022112075000377

Jackett, D. R., & McDougall, T. J. (1997). A neutral density variable for the world's oceans. *Journal of Physical Oceanography*, *27*(2), 237–263. https://doi.org/10.1175/1520-0485(1997)027<0237:ANDVFT>2.0.CO;2

Jiang, M., Measures, C. I., Barbeau, K. A., Charette, M. A., Gille, S. T., Hatta, M., et al. (2019). Fe sources and transport from the Antarctic Peninsula shelf to the Southern Scotia Sea. *Deep Sea Research Part I: Oceanographic Research Papers*, *150*, 103060. https://doi.org/10.1016/j.dsr.2019.06.006

Jones, D., Sonnewald, M., Zhou, S., Hausmann, U., Meijers, A. J. S., Rosso, I., et al. (2023). *Unsupervised classification identifies coherent thermohaline structures in the Weddell Gyre region* (pp. 1–40). EGUsphere. https://doi.org/10.5194/egusphere-2022-1484

Ledwell, J. R., Watson, A. J., & Law, C. S. (1993). Evidence for slow mixing across the pycnocline from an open-ocean tracer-release experiment. *Nature*, *364*(6439), 701–703. https://doi.org/10.1038/364701a0

Llort, J., Langlais, C., Matear, R., Moreau, S., Lenton, A., & Strutton, P. G. (2018). Evaluating southern ocean carbon eddy-pump from biogeochemical-Argo floats. *Journal of Geophysical Research: Oceans*, *123*(2), 971–984. https://doi.org/10.1002/2017JC012861

Martínez-Moreno, J., Hogg, A. M., England, M. H., Constantinou, N. C., Kiss, A. E., & Morrison, A. K. (2021). Global changes in oceanic mesoscale currents over the satellite altimetry record. *Nature Climate Change*, *11*(5), 397–403. https://doi.org/10.1038/s41558-021-01006-9

Meredith, M. P., Meijers, A. S., Naveira Garabato, A. C., Brown, P. J., Venables, H. J., Abrahamsen, E. P., et al. (2015). Circulation, retention, and mixing of waters within the Weddell-Scotia confluence, southern ocean: The role of stratified Taylor columns. *Journal of Geophysical Research: Oceans*, *120*(1), 547–562. https://doi.org/10.1002/2014JC010462

Meyer, A., Phillips, H. E., Sloyan, B. M., & Polzin, K. L. (2014). *Mixing (MX) Oceanographic Toolbox for EM-APEX float data applying shear-strain parameterisation* (p. 69). Hobart: University of Tasmania. Retrieved from https://www.mathworks.com/matlabcentral/fileexchange/47595-mixing-mx-oceanographic-toolbox-for-em-apex-float-data

Mohrmann, M., Swart, S., & Heuzé, C. (2022). Observed mixing at the flanks of Maud rise in the Weddell Sea. *Geophysical Research Letters*, *49*(8), e2022GL098036. https://doi.org/10.1029/2022GL098036

Nakamura, T., Awaji, T., Hatayama, T., Akitomo, K., Takizawa, T., Kono, T., et al. (2000). The generation of large-amplitude unsteady lee waves by subinertial K1 tidal flow: A possible vertical mixing mechanism in the Kuril straits. *Journal of Physical Oceanography*, *30*(7), 1601–1621. https://doi.org/10.1175/1520-0485(2000)030<1601:TGOLAU>2.0.CO;2

Naveira Garabato, A. C., Ferrari, R., & Polzin, K. L. (2011). Eddy stirring in the Southern Ocean. *Journal of Geophysical Research: Oceans*, *116*(C9), C09019. https://doi.org/10.1029/2010JC006818

Naveira Garabato, A. C. N., Polzin, K. L., King, B. A., Heywood, K. J., & Visbeck, M. (2004). Widespread intense turbulent mixing in the Southern Ocean. *Science*, *303*(5655), 210–213. https://doi.org/10.1126/science.1090929

Nicholls, K. W., Østerhus, S., Makinson, K., Gammelsrød, T., & Fahrbach, E. (2009). Ice-ocean processes over the continental shelf of the southern Weddell Sea, Antarctica: A review. *Reviews of Geophysics*, *47*(3). https://doi.org/10.1029/2007RG000250

Nikurashin, M., & Ferrari, R. (2010). Radiation and dissipation of internal waves generated by geostrophic motions impinging on small-scale topography: Application to the southern ocean. *Journal of Physical Oceanography*, *40*(9), 2025–2042. https://doi.org/10.1175/2010JPO4315.1

Oakey, N. S. (1982). Determination of the rate of dissipation of turbulent energy from simultaneous temperature and velocity shear microstructure measurements. *Journal of Physical Oceanography*, *12*(3), 256–271. https://doi.org/10.1175/1520-0485(1982)012<0256:DOTROD>2.0.CO;2

Orsi, A. H., Johnson, G. C., & Bullister, J. L. (1999). Circulation, mixing, and production of Antarctic bottom water. *Progress in Oceanography*, *43*(1), 55–109. https://doi.org/10.1016/S0079-6611(99)00004-X

Orsi, A. H., Whitworth, T., & Nowlin, W. D. (1995). On the meridional extent and fronts of the Antarctic circumpolar current Part I. *Deep-Sea Research*, *42*(5), 641–673. https://doi.org/10.1016/0967-0637(95)00021-w

Osborn, T. R. (1980). Estimates of the local rate of vertical diffusion from dissipation measurements. *Journal of Physical Oceanography*, *10*(1), 83–89. https://doi.org/10.1175/1520-0485(1980)010<0083:EOTLRO>2.0.CO;2

Osborn, T. R., & Cox, C. S. (1972). Oceanic fine structure. *Geophysical Fluid Dynamics*, *3*(4), 321–345. https://doi.org/10.1080/03091927208236085

Patterson, S. L., & Sievers, H. A. (1980). The weddell-scotia confluence. *Journal of Physical Oceanography*, *10*(10), 1584–1610. https://doi.org/10.1175/1520-0485(1980)010<1584:TWSC>2.0.CO;2

Perissinotto, R., & Duncombe Rae, C. M. (1990). Occurrence of anticyclonic eddies on the prince Edward plateau (Southern Ocean): Effects on phytoplankton biomass and production. *Deep-Sea Research, Part A: Oceanographic Research Papers*, *37*(5), 777–793. https://doi.org/10.1016/0198-0149(90)90006-H

Polzin, K. L., Garabato, A. C. N., Abrahamsen, E. P., Jullion, L., & Meredith, M. P. (2014). Boundary mixing in Orkney passage outflow. *Journal of Geophysical Research: Oceans*, *119*(12), 8627–8645. https://doi.org/10.1002/2014JC010099

Polzin, K. L., Toole, J. M., Ledwell, J. R., & Schmitt, R. W. (1997). Spatial variability of turbulent mixing in the abyssal ocean. *Science*, *276*(5309), 93–96. https://doi.org/10.1126/science.276.5309.93

Polzin, K. L., Toole, J. M., & Schmitt, R. W. (1995). Finescale parameterizations of turbulent dissipation. *Journal of Physical Oceanography*, *25*(3), 306–328. https://doi.org/10.1175/1520-0485(1995)025<0306:FPOTD>2.0.CO;2

Prend, C. J., Gille, S. T., Talley, L. D., Mitchell, B. G., Rosso, I., & Mazloff, M. R. (2019). Physical drivers of phytoplankton bloom initiation in the Southern Ocean's Scotia Sea. *Journal of Geophysical Research: Oceans*, *124*(8), 5811–5826. https://doi.org/10.1029/2019JC015162

Rintoul, S., Hughes, C. W., & Olbers, D. (2001). Chapter 4.6 the antarctic circumpolar current system. In G. Siedler, J. Church, & J. Gould (Eds.), *International geophysics* (Vol. 77, pp. 271–XXXVI). Academic Press. https://doi.org/10.1016/S0074-6142(01)80124-8

Rio, M. H., Guinehut, S., & Larnicol, G. (2011). New CNES-CLS09 global mean dynamic topography computed from the combination of GRACE data, altimetry, and in situ measurements. *Journal of Geophysical Research-Oceans*, *116*(C7), C07018. https://doi.org/10.1029/2010JC006505

Rippeth, T. P., Vlasenko, V., Stashchuk, N., Scannell, B. D., Green, J. A. M., Lincoln, B. J., & Bacon, S. (2017). Tidal conversion and mixing poleward of the critical latitude (an arctic case study). *Geophysical Research Letters*, *44*(24), 12–349. https://doi.org/10.1002/2017GL075310

Sanford, T. B. (1971). Motionally induced electric and magnetic fields in the sea. *Journal of Geophysical Research*, *76*(15), 3476–3492. https://doi.org/10.1029/JC076i015p03476

Sanford, T. B., Drever, R. G., & Dunlap, J. H. (1978). A velocity profiler based on the principles of geomagnetic induction. *Deep-Sea Research*, *25*(2), 183–210. https://doi.org/10.1016/0146-6291(78)90006-1

Sanford, T. B., Dunlap, J. H., Carlson, J. A., Webb, D. C., & Girton, J. B. (2005). Autonomous velocity and density profiler: EM-APEX. In *Proceedings of the IEEE/OES eighth working conference on current measurement technology* (pp. 152–156). https://doi.org/10.1109/CCM.2005.1506361

Schmit, R. W., Toole, J. M., Koehler, R. L., Mellinger, E. C., & Doherty, K. W. (1988). The development of a fine- and microstructure profiler. *Journal of Atmospheric and Oceanic Technology*, *5*(4), 484–500. https://doi.org/10.1175/1520-0426(1988)005<0484:TDOAFA>2.0.CO;2

Sévellec, F., Naveira Garabato, A. C., Brearley, J. A., & Sheen, K. L. (2015). Vertical flow in the southern ocean estimated from individual moorings. *Journal of Physical Oceanography*, *45*(9), 2209–2220. https://doi.org/10.1175/JPO-D-14-0065.1

Sheen, K. L., Brearley, J. A., Naveira Garabato, A. C., Smeed, D. A., Waterman, S., Ledwell, J. R., et al. (2013). Rates and mechanisms of turbulent dissipation and mixing in the southern ocean: Results from the diapycnal and isopycnal mixing experiment in the southern ocean (DIMES). *Journal of Geophysical Research: Oceans*, *118*(6), 2774–2792. https://doi.org/10.1002/jgrc.20217

Sherwin, T. J. (1988). Analysis of an internal tide observed on the malin shelf, North of Ireland. *Journal of Physical Oceanography*, *18*(7), 1035–1050. https://doi.org/10.1175/1520-0485(1988)018<1035:AOAITO>2.0.CO;2

Tamsitt, V., Drake, H. F., Morrison, A. K., Talley, L. D., Dufour, C. O., Gray, A. R., et al. (2017). Spiraling pathways of global deep waters to the surface of the southern ocean. *Nature Communications*, *8*(1), 172. https://doi.org/10.1038/s41467-017-00197-0

Thompson, A. F., & Sallée, J.-B. (2012). Jets and topography: Jet transitions and the impact on transport in the Antarctic circumpolar current. *Journal of Physical Oceanography*, *42*(6), 956–972. https://doi.org/10.1175/JPO-D-11-0135.1

Thurnherr, A. M., & Brearley, J. A. (2024). Microstructure data from JR18004 collected using Rockland vertical microstructure profiler, January-February 2019. https://doi.org/10.5285/1f13965c-8aa4-ea6e-e063-7086abc04b0f

Thurnherr, A. M., Clément, L., Laurent, L. S., Ferrari, R., & Ijichi, T. (2020). Transformation and upwelling of bottom water in fracture zone valleys. *Journal of Physical Oceanography*, *50*(3), 715–726. https://doi.org/10.1175/JPO-D-19-0021.1

Thurnherr, A. M., & Middleton, L. (2024). Lowered acoustic Doppler current profiler (LADCP) data from cruise JR18004. https://doi.org/10.5285/1fbb7874-5433-3b07-e063-7086abc0bee9

Troupin, C., Beltran, J. P., Heslop, E., Torner, M., Garau, B., Allen, J., et al. (2015). A toolbox for glider data processing and management. *Methods in Oceanography*, *13–14*, 13–23. https://doi.org/10.1016/j.mio.2016.01.001

Vernet, M., Geibert, W., Hoppema, M., Brown, P. J., Haas, C., Hellmer, H. H., et al. (2019). The Weddell gyre, southern ocean: Present knowledge and future challenges. *Reviews of Geophysics*, *57*(3), 623–708. https://doi.org/10.1029/2018RG000604

Vlasenko, V., Stashchuk, N., & Hutter, K. (2005). *Baroclinic tides: Theoretical modeling and observational evidence*. Cambridge University Press. https://doi.org/10.1017/CBO9780511535932

Weatherall, P., Marks, K. M., Jakobsson, M., Schmitt, T., Tani, S., Arndt, J. E., et al. (2015). A new digital bathymetric model of the world's oceans. *Earth and Space Science*, *2*(8), 331–345. https://doi.org/10.1002/2015EA000107

Whitworth, T., Nowlin, W. D., Orsi, A. H., Locarnini, R. A., & Smith, S. G. (1994). Weddell Sea shelf water in the bransfield strait and weddell-scotia confluence. *Deep Sea Research Part I: Oceanographic Research Papers*, *41*(4), 629–641. https://doi.org/10.1016/0967-0637(94)90046-9

Zhou, S., Meijers, A. J. S., Meredith, M. P., Abrahamsen, E. P., Holland, P. R., Silvano, A., et al. (2023). Slowdown of Antarctic Bottom Water export driven by climatic wind and sea-ice changes. *Nature Climate Change*, *13*(7), 701–709. https://doi.org/10.1038/s41558-023-01695-4